AD-A243 725

CALCULATIONS OF ELECTRON AND PHOTON TRANSPORT BETWEEN 1 MeV and 1 eV

Arcon Corporation

Stanley Woolf
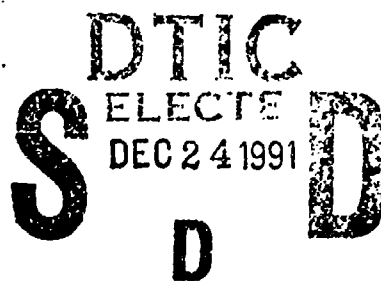
DTIC
ELECTE
DEC 2 4 1991
S D
D

91-18783

91

This report has been reviewed by the Rome Laboratory Public Affairs Division (PA) and is releasable to the National Technical Information Service (NTIS). At NTIS it will be releasable to the general public, including foreign nations.

RL-TR-91-289 has been reviewed and is approved for publication.

APPROVED: *John Garth*

JOHN GARTH
Project Engineer

FOR THE COMMANDER: *Harold Roth*

HAROLD ROTH, Director
Solid State Sciences Directorate

If your address has changed or if you wish to be removed from the Rome Laboratory mailing list, or if the addressee is no longer employed by your organization, please notify Rome Laboratory (ERT) Hanscom AFB MA 01731-5000. This will assist us in maintaining a current mailing list.

Do not return copies of this report unless contractual obligations or notices on a specific document require that it be returned.

REPORT DOCUMENTATION PAGE

Public reporting burden for this collection of information is estimated to average 1 hour per response, including the time for reviewing instructions, searching existing data sources, gathering and maintaining the data needed, and completing and reviewing the collection of information. Send comments regarding this burden estimate or any other aspect of this collection of information, including suggestions for reducing this burden, to Washington Headquarters Services, Directorate for Information Operations and Reports, 1215 Jefferson Davis Highway, Suite 1204, Arlington, VA 22202-4302, and to the Office of Management and Budget, Paperwork Reduction Project (0704-0188), Washington, DC 20503

1. AGENCY USE ONLY (Leave Blank)	2. REPORT DATE	3. REPORT TYPE AND DATES COVERED
	November 1991	Final Jul 86 - Aug 89

4. TITLE AND SUBTITLE	5. FUNDING NUMBERS
CALCULATIONS OF ELECTRON AND PHOTON TRANSPORT BETWEEN 1 MeV and 1 eV	C - F19628-86-C-0019
	PE - 61102F
6. AUTHOR(S)	PR - 2306
	TA - J3
Stanley Woolf	WU - 35

7. PERFORMING ORGANIZATION NAME(S) AND ADDRESS(ES)	8. PERFORMING ORGANIZATION REPORT NUMBER
Arcon Corporation 260 Bear Hill Road Waltham MA 02154	N/A

9. SPONSORING/MONITORING AGENCY NAME(S) AND ADDRESS(ES)	10. SPONSORING/MONITORING AGENCY REPORT NUMBER
Rome Laboratory (ERT) Hanscom AFB MA 01731-5000	RL-TR-91-289

11. SUPPLEMENTARY NOTES
Rome Laboratory Project Engineer: John C. Garth/ERT/(617) 377-2360

12a. DISTRIBUTION/AVAILABILITY STATEMENT	12b. DISTRIBUTION CODE
Approved for public release; distribution unlimited.	

13. ABSTRACT (Maximum 200 words)

In this report we describe the development and implementation of numerical methods for the simulation and description of electron and photon transport in layered one-dimensional structures such as metallized semiconductors. The simulations described were used to calculate charge distributions and predict from 1 eV to 20 MeV. The scope of our work included: 1) discrete ordinates transport calculations and dose predictions for primary and secondary electrons and for bremsstrahlung photons in one-dimensional layered media; 2) Monte Carlo electron transport and dose calculations in one- two- and three-dimensions; 3) implementation of electron-photon scattering theory in Monte Carlo and discrete ordinates simulation of low energy 8.9eV electron transport in SiO_2.

14. SUBJECT TERMS		15. NUMBER OF PAGES
Electron transport; coupled electron-photon transport; photon transport; charge distributions in insulators; electron-photon interactions		80
		16. PRICE CODE

17. SECURITY CLASSIFICATION OF REPORT	18. SECURITY CLASSIFICATION OF THIS PAGE	19. SECURITY CLASSIFICATION OF ABSTRACT	20. LIMITATION OF ABSTRACT
UNCLASSIFIED	UNCLASSIFIED	UNCLASSIFIED	UL

TABLE OF CONTENTS

I. INTRODUCTION

During the period from July 1, 1986 through August 31, 1989, the execution of contract No. F19628-86-C-0019 was directed toward the development and implementation of numerical methods for simulating and describing the transport of electrons and photons in layered one-dimensional and multiregion two- and three-dimensional structures such as metallized semiconductors. In addition to microelectronic device structures, the numerical methods developed were also applied to liquid media (i.e. H_2O). The transport simulations were used to calculate charge distributions and to predict dose distributions in these media, resulting from electron beams and sources of x- and gamma irradiation. Another important aspect of the electron transport calculation activity during this contract was the extension of the range of our simulation capability to electron-phonon scattering. The effects of this interaction and the effect of the presence of applied electric fields on the energy spectra and spatial distribution of electrons in SiO_2 were examined, with particular attention to the promotion of electron energies from the subionization region to energies above the ionization threshold and the resulting electron multiplication. Some of the results of the electron and photon transport calculations are reported in seven technical papers in which the principal investigator shared authorship.

The electron and photon transport calculations were made using the method of discrete ordinates and the Monte Carlo trajectory simulation method. The discrete ordinates calculations were made using the ONETRAN[1] computer code. With this code we calculated: (1) charge distributions and energy deposition in nine materials due to the incidence of monodirectional electron sources for several energies and incident angles; (2) electron and photon transport in H_2O; (3) energy deposition in and electron transmission energy spectra from Al for the purpose of comparison with independent transport calculations made using the method of streaming rays. The Monte Carlo method was used to perform electron transport calculations in one-, two- and three-dimensions. Most of the Monte Carlo calculations involved the use of the ITS[2] code series. However, some of the one-dimensional calculations were performed with Monte Carlo programs which we wrote expressly for the purpose: in particular an electron transport calculation to test a new scattering cross section formulation; and an electron-phonon scattering simulation.

1

This report is organized into five sections in addition to this, the introduction. Section II is a discussion and presentation of results of one-dimensional discrete ordinates calculations of electron and photon transport. Section III presents the results of electron transport Monte Carlo calculations in one-, two- and three-dimensions and shows comparisons of these results with transport solutions obtained by other methods. Section IV consists of a discussion of electron-phonon scattering and some of the results obtained with our Monte Carlo simulation of electron transport in the 1 to 20 eV energy range. Section V is a discussion of the formulation of and progress made towards a discrete ordinates solution to the electron transport problem in the 1 to 20 eV energy range. The final section, VI, is a list of the references cited throughout this report.

II. DISCRETE ORDINATES CALCULATIONS OF ELECTRON AND PHOTON TRANSPORT IN ONE-DIMENSION

1. Introduction

Prior to the start of this reporting period, we had acquired a substantial amount of experience in adapting the multigroup, discrete ordinates method to the calculation of electron energy deposition profiles and electron flux distributions in several materials. In view of this, it was deemed appropriate, during the performance of this contract, to perform a systematic study of the range of validity of this method. The conclusions reached as a result of performing this work were: 1) that the simple continuous-slowing-down approximation (CSDA) electron transport model was adequate for electron transport calculations in the energy range 100 keV to ~1.5 MeV for a wide range of scattering materials; and 2) above this energy range, the CSDA proved inadequate. This second conclusion led to an extensive amount of effort to account for radiative energy losses and knock-on secondary electron production in our transport calculations. To account for these two electron energy loss mechanisms, we began an effort to apply the discrete ordinates method to electron-photon transport. We shall first discuss the results of the application of the method of discrete ordinates, incorporating only the CSDA model, to the determination of electron energy deposition and charge distributions in several materials. Following this will be a discussion of our application of the discrete ordinates method to electron-photon transport.

2. Application of the Discrete Ordinates Method to Electron Transport in the 0.1 - 1.4 MeV Energy Range

The multigroup discrete ordinates code ONETRAN[1] was used to calculate energy deposition profiles and charge distributions in a number of solids due to the incidence of electron beams ranging in energy from 0.1 to 1.4 MeV. In these calculations electron energy loss was allowed only through application of the continuous-slowing-down approximation (CSDA). Thus energy downscatter was allowed only between adjacent energy groups. Energy losses through radiative processes or through catastrophic (knock-on) collisions were not considered. The primary motivation for this study was to determine the range of validity of the method of discrete ordinates under the above straightforward assumptions. The transport calculations were made for several materials over a wide range of atomic numbers (Z=4 - 92). A large body of data[3,4], experimental measurements and Monte Carlo calculations of energy deposition, was available to us for comparison purposes. Some of the results obtained will be

3

presented here. However, the complete body of results and comparisons, consisting of 3 flux plots, 14 energy deposition plots, a transmission spectrum and a reflection spectrum, is presented in Ref. 5.

Since the basic principles of the discrete ordinates method are presented briefly in Ref. 5 and extensively elsewhere (e.g. Ref.6), it is sufficient to state here that in the multigroup approximation, the electron energy range is divided into a number of energy groups of width ΔE_g: the monoenergetic transport equation is then solved for each energy group flux, ϕ_g, with the removal cross section σ_{ag} for group g given by CSDA as

$$\sigma_{ag} = S(E_g)/\Delta E_g, \tag{1}$$

where $S(E_g)$ is the collision stopping power for electrons with energy E_g. If the group structure is arranged such that increasing group index g corresponds to decreasing energy, then the electrons removed from group g, $\sigma_{ag}\phi_g$, become the inscatter source to group $g+1$. The group flux, ϕ_g, is a function of position and angle. The angular dependence is treated by resolving the flux into a number of angular components, each corresponding to a particular discrete ordinate, and then solving the transport equation for each of these components. The spatial(x) dependence of the flux is solved for by the use of the diamond difference approximation, or in the case of ONETRAN, the linear discontinuous finite element approximation.

If we define the angular flux along a particular discrete ordinate, say μ_i, as $\phi_{ig}(x)$, then we can, by integration over angle, obtain the group scalar flux $\phi_g(x)$. If the integration is performed numerically, then

$$\phi_g(x) = \sum_{i=1}^{M} w_i \phi_{ig}(x) , \tag{2}$$

where the w_i are the numerical quadrature weights corresponding to the discrete ordinate direction μ_i. A sample plot of $\phi_g(x)$ is shown in Fig. 1 for the case of a 1 MeV monodirectional electron source, incident direction $\mu_0 = 1.0$, located at $x = 0$ in an infinite medium of Be(Z=4). The ONETRAN calculation was made for 200 energy groups of equal width. Shown in Fig. 1 are the group scalar fluxes, as a function of distance, for every tenth group, beginning with a top energy of 0.95 MeV. From a figure such as this one can gain an appreciation for the change in the spatial characteristics of the charge distribution as the electron energy decreases. In Ref. 5 other scalar flux plots are given for 1 MeV electron in

higher Z materials. Fe(Z=26) and Ta(Z=73).
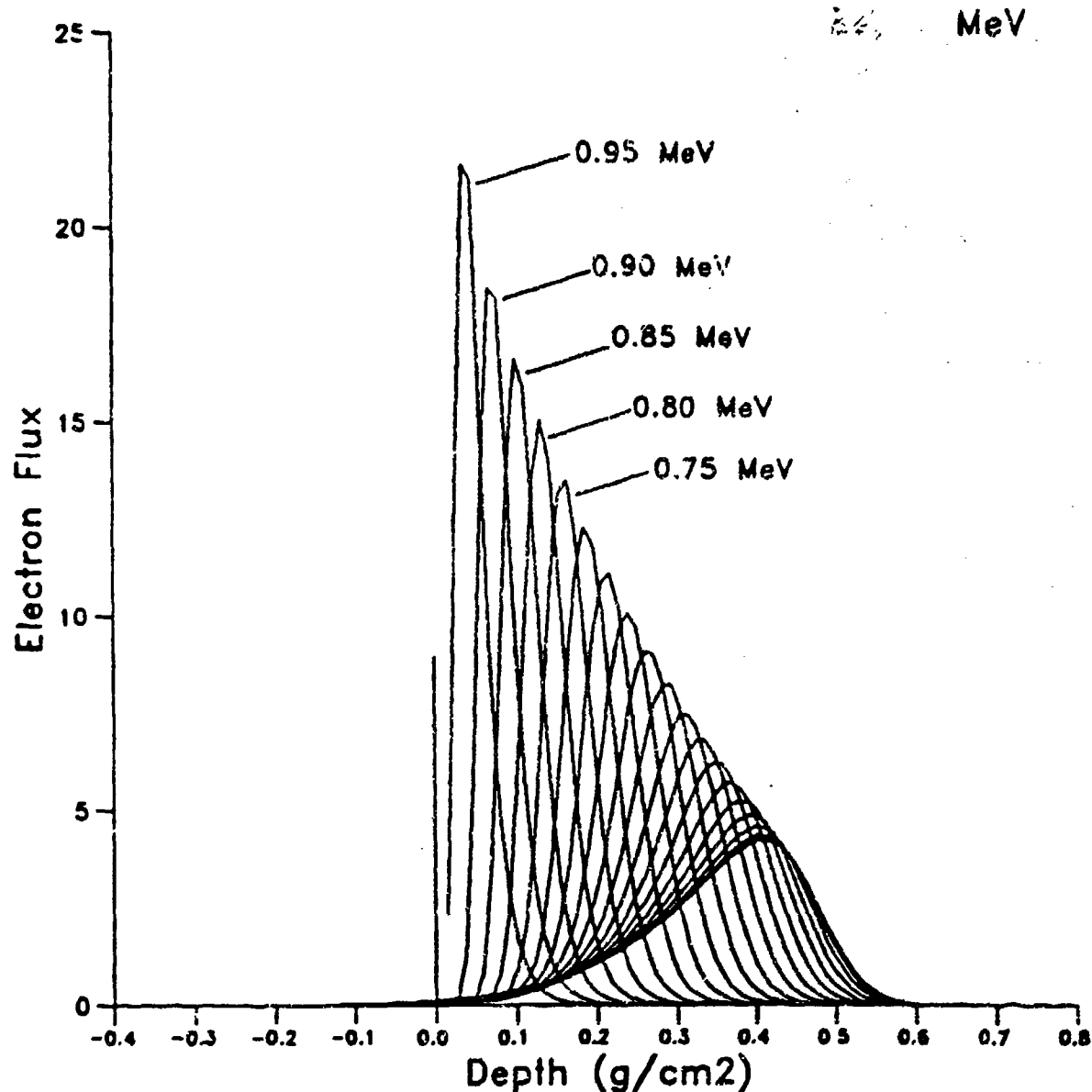
Figure 1. Electron group scalar flux, as calculated with ONETRAN[1], in an infinite medium of Be for 1 MeV electrons incident at an angle of 0° (Ref. 5) .

From these it can be observed that the directionality of the source electrons is sooner "forgotten" in the high Z materials than in materials of lower Z. Since the scattering in low Z materials is more anisotropic than for high Z, the electrons approach diffusive behavior sooner (at higher energy) than in low Z materials.

The energy deposition profile $W(x)$ is calculated as

$$W(x) = \sum_{g=1}^{G} \varphi_g(x) \, S(E_g) + \varphi_0(x) \, S(E_0) \, ,\qquad\qquad (3)$$

where $\varphi_0(x)$ is the unscattered flux at the source energy E_0, and G is the total number of groups. Typical energy deposition profile plots are shown in Figs. 2, 3 and 4. In all three of these figures we compare our ONETRAN result (solid curve) with the Monte Carlo calculation (histogram) and experimental calorimetric measurements(circles) of Lockwood, Miller and Halbleib[3]. In Fig. 2, the energy deposition is plotted for a 0.1 MeV electron beam normally incident on Be. The agreement with Monte Carlo is good, but not perfect. The agreement with experiment is not very good, but then neither is the agreement between experiment and Monte Carlo. Fig. 3 shows the energy deposition results for a slant beam (60°) of 0.5 MeV electrons incident on Mo. The overall agreement among the three methods is much better in this case. The results of a ONETRAN calculation for a three-layered scattering medium (Al/Au/Al) is shown in Fig. 4. A 1.0 MeV electron beam is normally incident on the vacuum boundary of the leftmost layer (Al). As can be seen, the agreement is very good.

3. Extension of the Discrete Ordinates Method to Coupled Electron-Photon Transport in the 1 MeV - 20 MeV Energy Range

As was stated in the above section, very good agreement with experimental and Monte Carlo energy deposition data was achieved for electron sources in the energy range 0.1 to 1.4 MeV. In the one high energy case that we treated in Ref. 5, the 20 MeV electron beam incident on H_2O, the energy deposition profile obtained did not agree well with Monte Carlo results[7] (see Fig. 5). It became apparent that for high electron source energies, it would be necessary to include consideration of radiative energy losses in our calculations. The success of the coupled electron-photon S_n calculations performed by Lorence, Nelson and Morel[8] for isotropic electron sources provided us with sufficient encouragement to perform a set of calculations for high energy electron beam sources, in particular to repeat the 20 MeV-H_2O calculation. The technique developed would then be applied to other beam energies in H_2O and other materials as well. We installed a bremsstrahlung photon production and transport module into our code.

6

Figure 2. Energy deposition, as calculated with ONETRAN[1], in semi-infinite Be for 0.1 MeV electrons incident at an angle of 0° (Ref. 5). Circles (experiment) and histogram (Monte Carlo) data taken from Ref. 4.
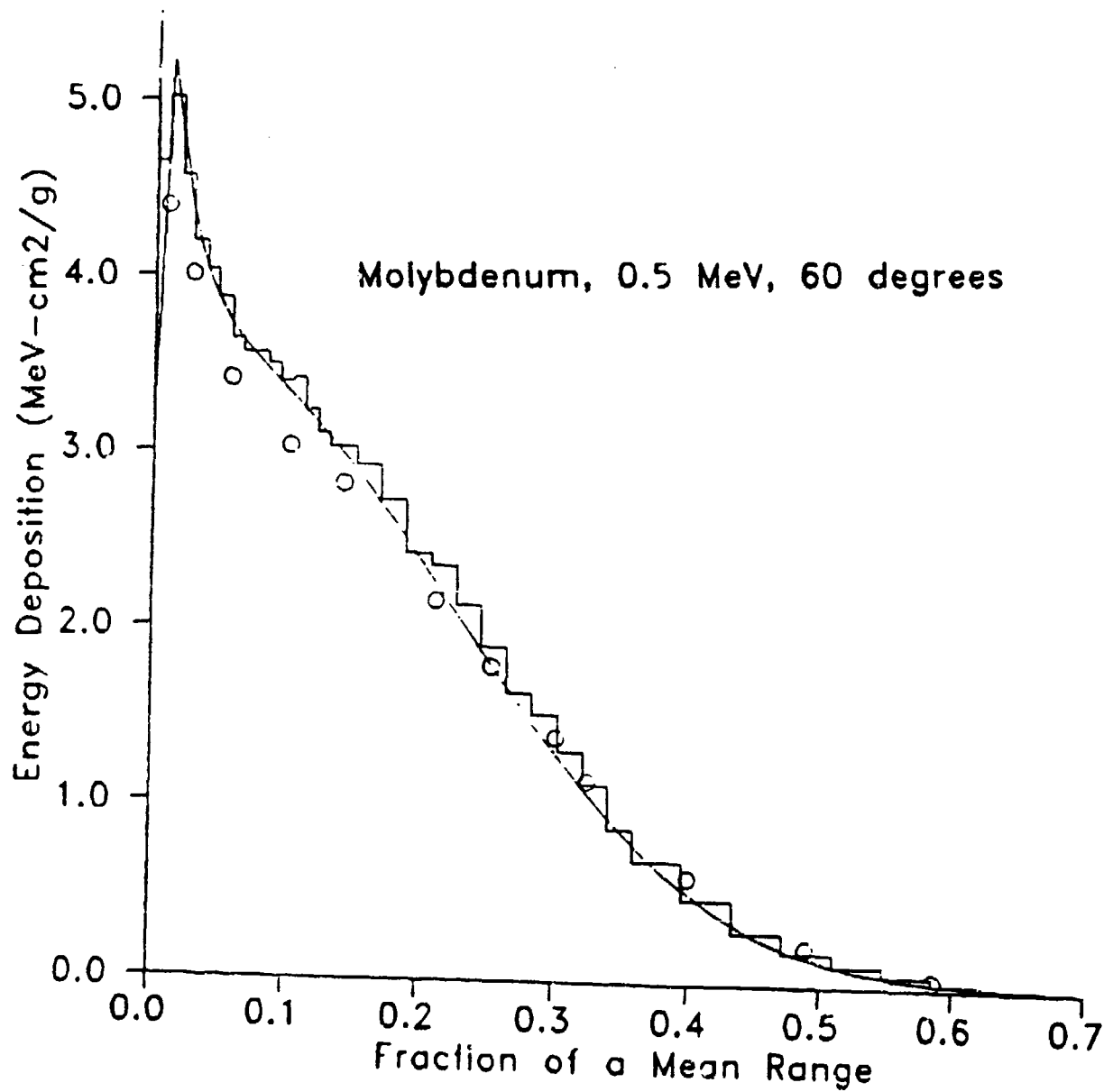
Figure 3. Energy deposition, as calculated with ONETRAN[1], in semi-infinite Mo for 0.5 MeV electrons incident at an angle of 60° (Ref. 5). Circles (experiment) and histogram (Monte Carlo) data taken from Ref. 4.
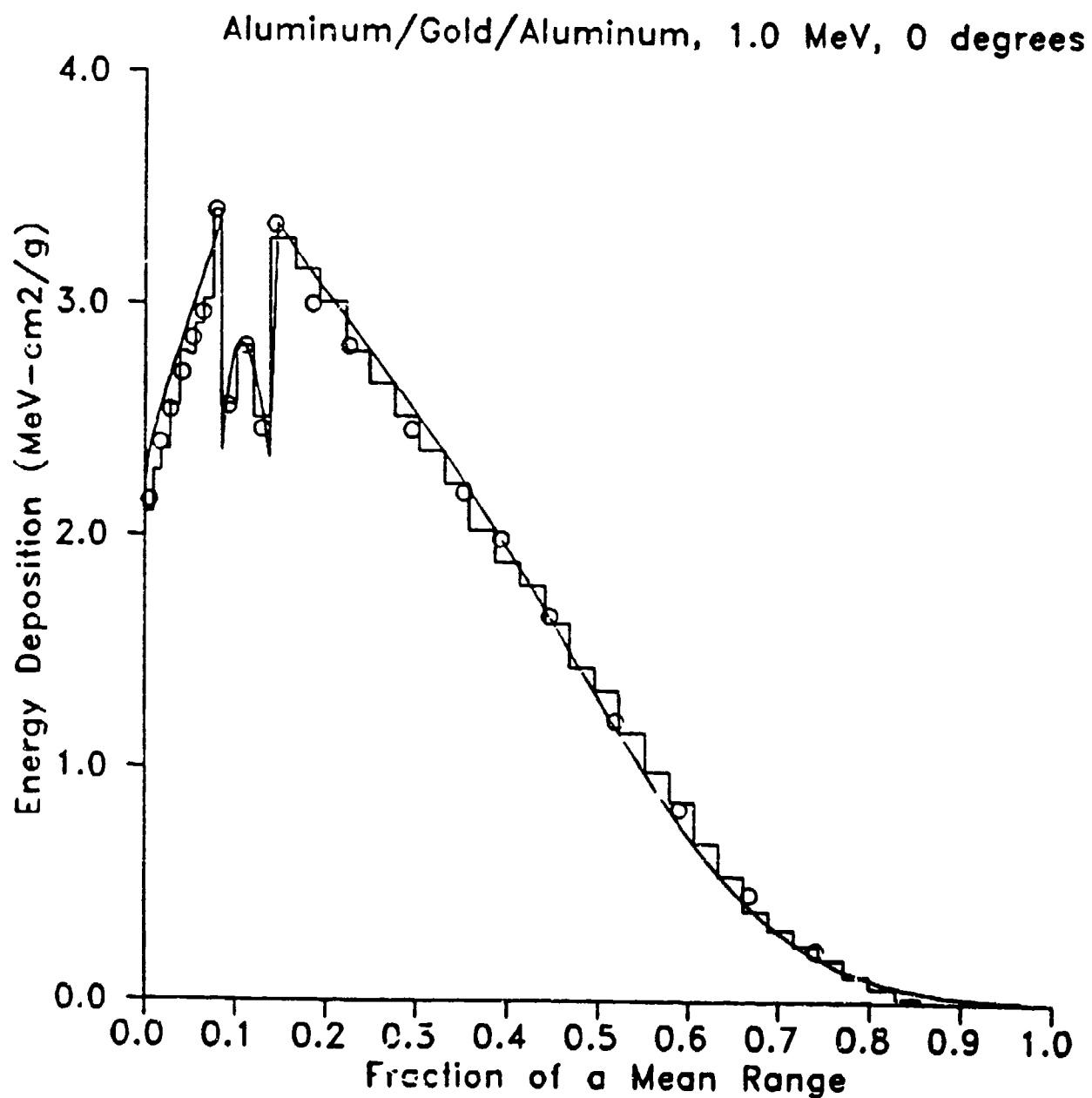
Figure 4. Energy deposition, as calculated with ONETRAN[1], in a Al/Au/Al configuration for 1.0 MeV electrons incident at an angle of 0° (Ref. 5). Circles (experiment) and histogram (Monte Carlo) data taken from Ref. 4.
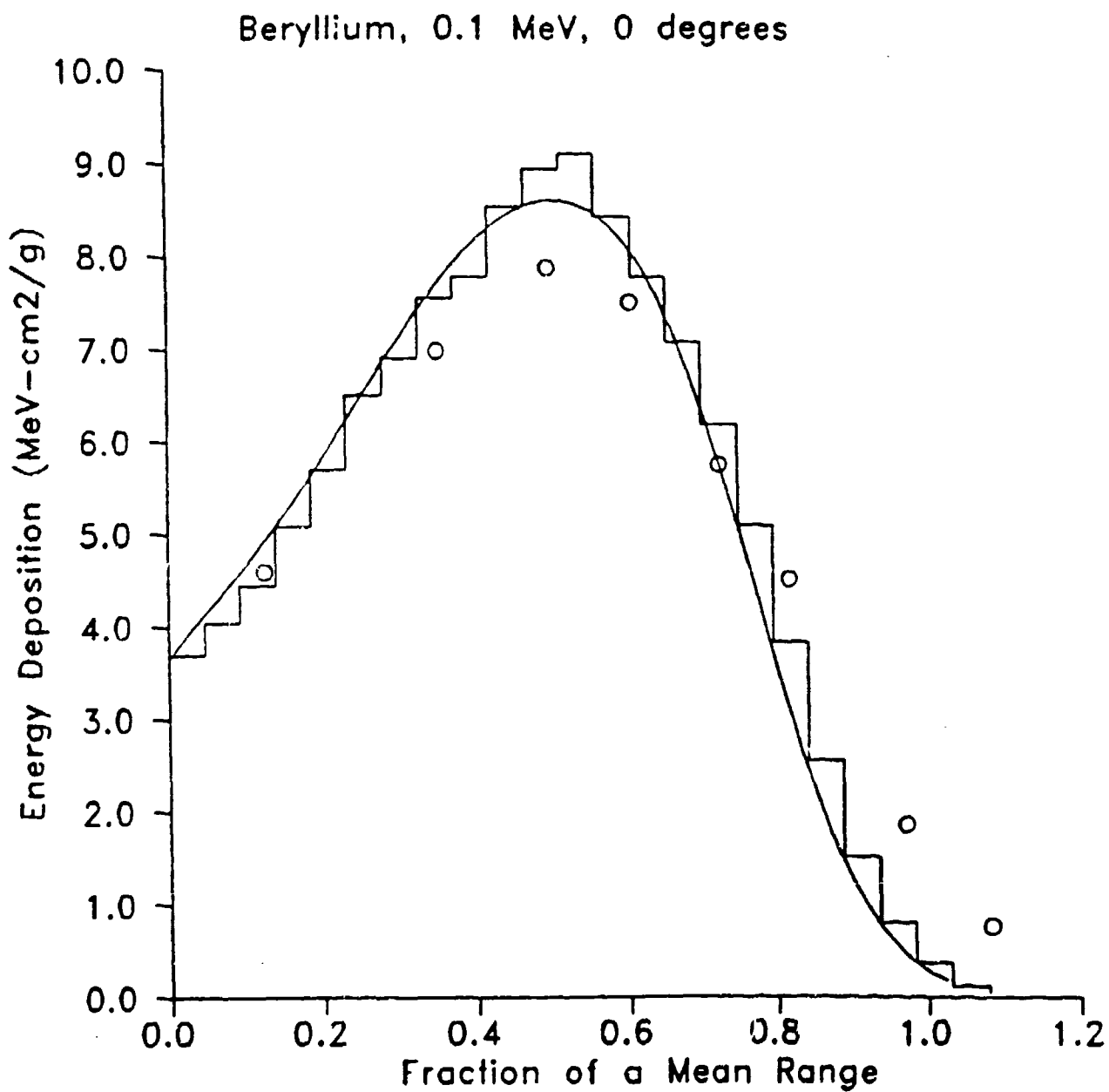
9
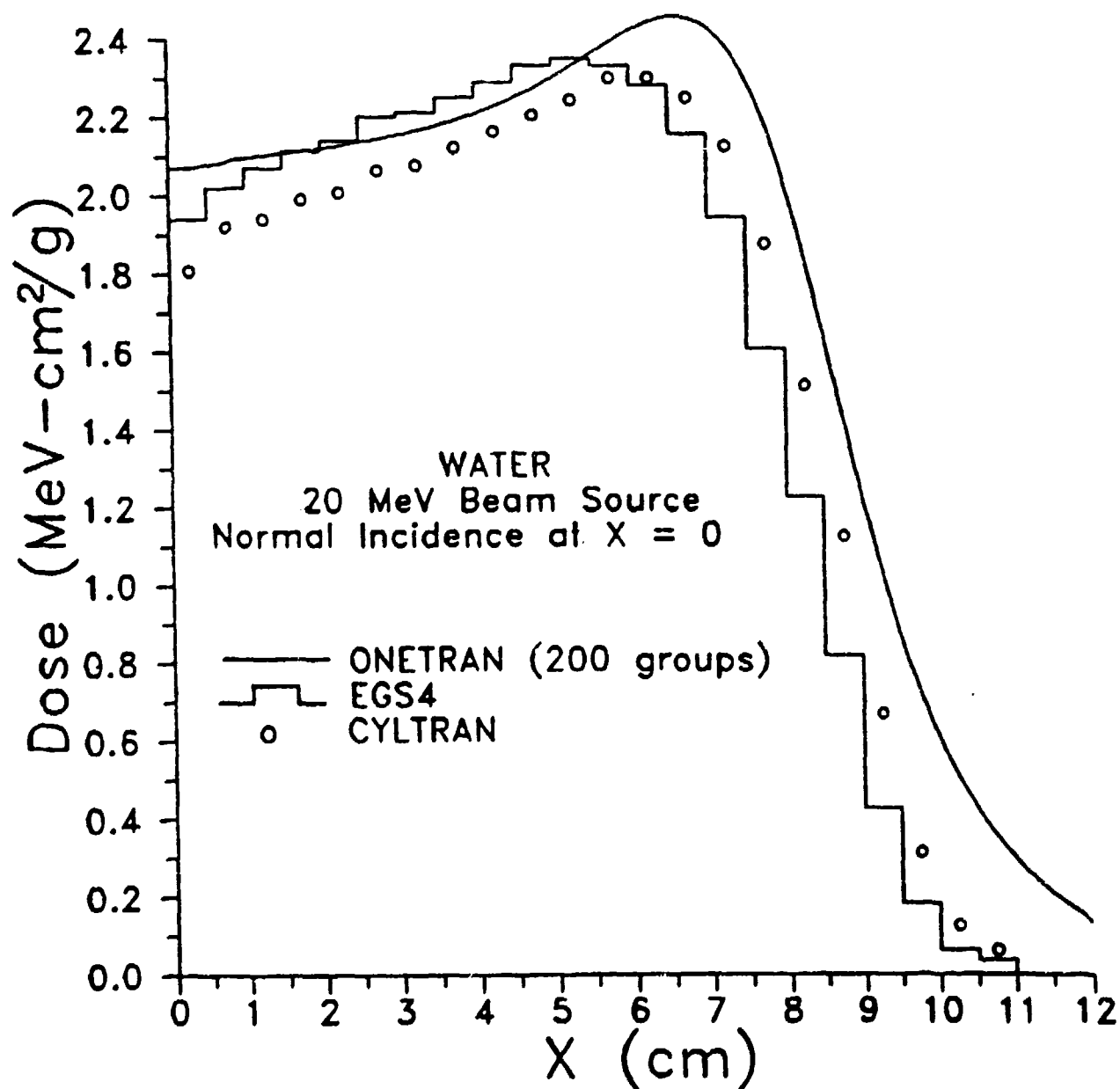
Figure 5. Energy deposition. as calculated with ONETRAN[1], in semi-infinite H$_2$O for 20 MeV electrons incident at an angle of 0° (Ref. 5). Circles (experiment) and histogram (Monte Carlo) data taken from Ref. 7.

3.1 Electron Energy Loss Cross Sections

In our previous calculations it was assumed that electron energy loss was adequately described by the continuous slowing down approximation (CSDA). In the multigroup S_n formulation, energy downscatter of electrons was allowed to occur only between adjacent energy groups. This simplifying assumption led to the use of a version of the ONETRAN code much smaller in size and complexity than the original. Inclusion of radiative energy losses necessitated the use of the full ONETRAN capability to allow for energy downscatter between any two groups. As for the radiative energy loss cross sections, we performed our early calculations with a very approximate elementary treatment[9], subsequently improved, for the bremsstrahlung generation cross sections which proceeded as follows:

the differential cross section for the emission of a photon with energy between k($=h\nu$) and k+dk by an electron with kinetic energy E as it passes through a scattering medium is given by

$$\frac{d\sigma_{rad}}{dk} = N\frac{\sigma_o B Z^2}{k}\left(\frac{E + m_o c^2}{E}\right) \quad , \qquad (cm^{-1}) \qquad (4)$$

where σ_o is a constant,

     B is a slowly varying function of E,

     Z is the atomic number of the scattering medium,

     $m_o c^2$ is the electron rest energy (all energies are expressed in MeV),

     N is the number of atoms/cm^3.

The radiative stopping power (electron radiative energy loss per unit path length) is defined as

$$\left(-\frac{dE}{ds}\right)_{rad} = N\int_0^E k d\sigma_{rad} \quad . \qquad (MeV/cm) \qquad (5)$$

Substituting Eq.(4) into Eq. (5),

$$\left(-\frac{dE}{ds}\right)_{rad} = N\sigma_0 Z^2(E + m_o c^2)\int_0^1 B \, d(k/E)$$

$$= N\sigma_0 Z^2(E + m_o c^2)\bar{B} \quad , \qquad (6)$$

where
$$\bar{B} \equiv \int_0^1 B \, d(k/E) \qquad (7)$$

11

is the average value of B over the allowed photon energy range.

If the parameter B of Eq.(4) is sufficiently slowly varying, we may approximate it as

$$B \approx \overline{B} \ . \tag{8}$$

Then Eq.(4) becomes

$$\frac{d\sigma_{rad}}{dk} \approx N \frac{\sigma_o \overline{B} Z^2}{k} \left(\frac{E + m_o c^2}{E} \right) \ ,$$

or

$$d\sigma_{rad} \approx \frac{1}{E} \left(-\frac{dE}{ds} \right)_{rad} \frac{dk}{k} \ . \qquad (cm^{-1}) \tag{9}$$

Eq. 9 formed the basis for our early calculations of multigroup bremsstrahlung cross sections. Numerical evaluation of the radiative stopping power was facilitated for us by the fact that the DATPAC[2] program calculates this quantity for arbitrary E and Z, and we had already adapted the DATPAC program to supply the Mott and Riley scattering cross sections for electrons.

The preponderance of literature pertaining to the calculation of bremsstrahlung cross sections[10-13] was a strong indication that the accuracy of our coupled electron-photon calculations might be significantly improved by the use of a more sophisticated bremsstrahlung cross section model than that given above. By fortunate circumstance, the DATPAC program incorporates much of the physics formulated in the Koch and Motz[10] paper and provides tabulations of the differential cross section ($k d\sigma_{rad}/dk$) as a function of electron energy E for arbitrary E and Z values. We extracted this data from DATPAC. In Fig. 6 we made a log-log plot of ($d\sigma_{rad}/dk$) vs. k for the top ten electron energy groups in a 100 group ONETRAN calculation where we took the electron source energy to be a 20 MeV beam incident on H_2O. Thus the ten curves correspond to electron energies ranging from 19.9 to 18.1 MeV in 0.2 MeV increments. The points indicate the tabulated values from DATPAC. While the curves are themselves difficult to read, we concluded from this plot and others similar to it, that the bremsstrahlung cross section could be easily approximated by straight lines (on log-log scale) connecting the points calculated by DATPAC. Thus, our approximation algorithm for ($d\sigma_{rad}/dk$) is of the form

$$\frac{d\sigma_{rad}}{dk} \approx A \, k^b, \tag{10}$$

where A and b are constant between any pair of points calculated by DATPAC. A unique determination of A and b is made for each point pair.

12

In our coupled electron-photon transport calculation, the multigroup cross sections for energy downscatter of electrons by radiative energy loss were calculated as follows: given an electron energy group structure (as shown in Fig. 7, with G uniformly spaced electron energy groups, each characterized by midpoint energy E_j (where $E_j > L_{j-1}$), then the cross section for emission of a photon with energy k ($= h\nu$) between k_1 and k_2, say, is

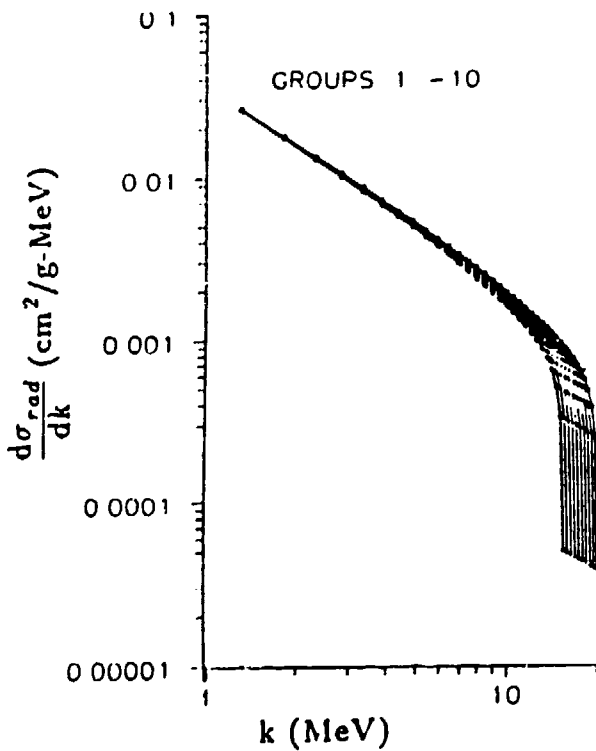$$\sigma_g(k) = \int_{k_1}^{k_2} \left(\frac{d\sigma_{rad}}{dk}\right) dk \quad .$$

(11)

Fig. 6. Differential bremsstrahlung cross section for 10 electron energies [19.9-18.1(.2)MeV] as calculated by DATPAC[2]
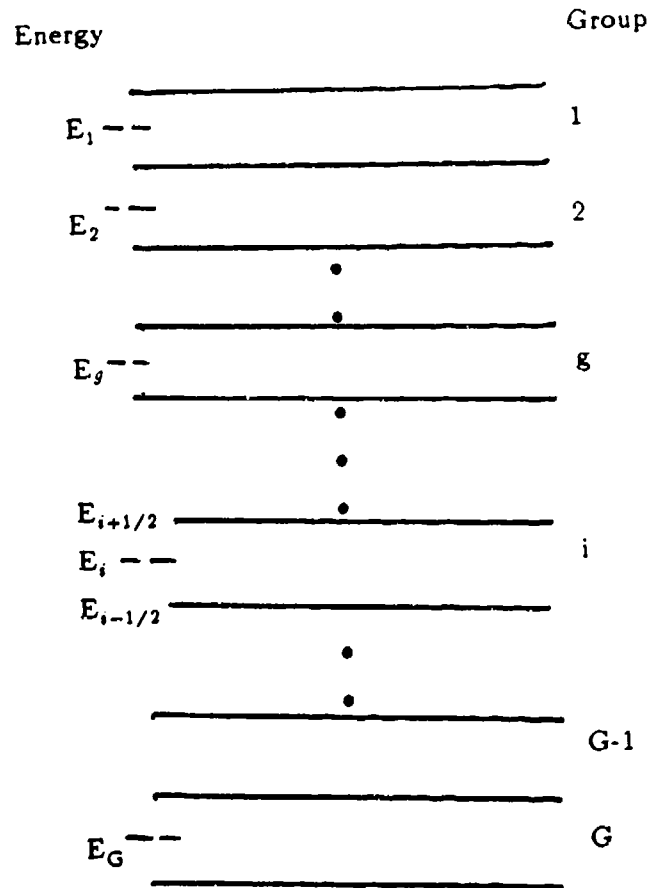
Fig.7. Electron energy group structure

If we assume that the energy of the electron after photon emission is E_1, then the limits of the integral are

13

$$k_1 = E_g - E_{i+1/2}.$$ (12a)

$$k_2 = E_g - E_{i-1/2} .$$ (12b)

or $(E_g - E_{i+1/2}) \leq k \leq (E_g - E_{i-1/2})$. (12c)

where $E_{i+1/2}$ and $E_{i-1/2}$ are the upper and lower energy bounds of group i.

It may then be said that the downscatter cross section from group g to group i due to the emission of a photon with energy between k_1 and k_2 is

$$\sigma_{g \to i}^{rad} = \sigma_g(k) ,$$ (13)

where $\sigma_g(k)$ is calculated from Eqs. 10 and 11 above.

3.2 Bremsstrahlung Photon Source

In addition to providing the means by which the electron downscatter due to radiative energy loss could be incorporated into the S_n calculation, the cross sections, $\sigma_{g \to i}^{rad}$, were used to determine the photon source function. The procedure we followed was: 1) perform the electron transport calculation with the ONETRAN S_n code; 2) retain a file of electron fluxes as functions of energy (group) and position; 3) calculate the photon source for use in a subsequent photon transport calculation; 4) perform the photon transport calculation with ONETRAN using multigroup photon cross sections which we generated with the GAMLEG code[14]; 5) calculate deposition profiles from both the electron (using flux file from step 1 and collision stopping powers) and photon contributions(using photon flux file from step 4 and energy absorption coefficients computed by GAMLEG). The energy group structure for the electron transport calculation was taken to be uniform, that is $\Delta E_i = E_i - E_{i+1}$ for all i. The photon energy group spacing was taken to be uniform for some calculations and logarithmic for others. The transport calculations were carried out for H_2O, and for the source energies considered, the energy lost to radiation was generally a small fraction of the total energy loss by the electrons. We found that our results were insensitive to the photon energy group structure, possibly due to the small overall radiative energy contribution. Also for this reason, we determined that a second electron transport calculation arising from the presence of Compton and photo-electrons would not significantly alter the results.

We made considerable modifications to the original version of the photon cross section calculation program GAMLEG[14]. The original version, published in 1969, was written in FORTRAN IV and incorporated a set of Biggs-Lighthill coefficients[15a,b] compiled in 1966. We updated the coding to FORTRAN-77 and incorporated the latest available set of Biggs-Lighthill coefficients[15c] and approximation algorithms for the cross sections. Also in the original version the photon cross sections could be calculated for up to 20 elements per run. We changed the code so that it now computes cross sections for an arbitrarily large (user-specified) number of chemical elements. We configured the code is now configured so that for a chemical compound, we enter as input the chemical symbol and weight fraction for each constituent element. The new input data structure, as we configured it, is identical to that implemented in the ITS code system.

3.3 Results for 5 MeV and 20 MeV Electron Beam sources

Figures 8 and 9 show the energy deposition results obtained with a 100 group coupled ONETRAN calculation for a 5 MeV electron beam normally incident on H_2O. The "slab" thickness for the electron calculation was taken to be 3 cm (the range of 5 MeV electrons in H_2O is 2.6 cm.). The depth of the scattering medium was extended to 10 cm. for the photon calculation to account for the backscatter of photons transported, due to their long mean free path, beyond 3 cm. In Figure 8 the total (electron + photon) energy deposition profile calculated with the ONETRAN code (solid curve) is compared with a TIGER[2] Monte Carlo calculation (histogram). The agreement between ONETRAN and TIGER is good, with the exception of the region between 1.25 and 1.8 cm. The electron beam source energy of 5 MeV pretty much delineates the point where errors due to numerical straggling become noticable. We believe that the consistently higher ONETRAN result shown between 1.25 and 1.8 cm. is primarily caused by numerical straggling, an error source caused by using the multigroup energy discretization scheme which is first-order accurate. As will be seen, this effect shows up more prominently as the source energy is increased. In Figure 9 we have plotted the energy deposition contribution of the bremsstrahlung photons for the 5 MeV electron source case. The agreement is generally good, although the TIGER histogram indicates that not enough histories were run to achieve statistical reliability. As can be seen from the photon dose scale, the maximum photon dose contribution is approximately 0.15% of the maximum electron dose contribution. For the electron transport, a 20 term extended transport corrected scattering cross section was used in an S_{20} ONETRAN calculation. For the photon transport, a P_4 scattering cross section model was used in an S_{20} ONETRAN calculation.

15
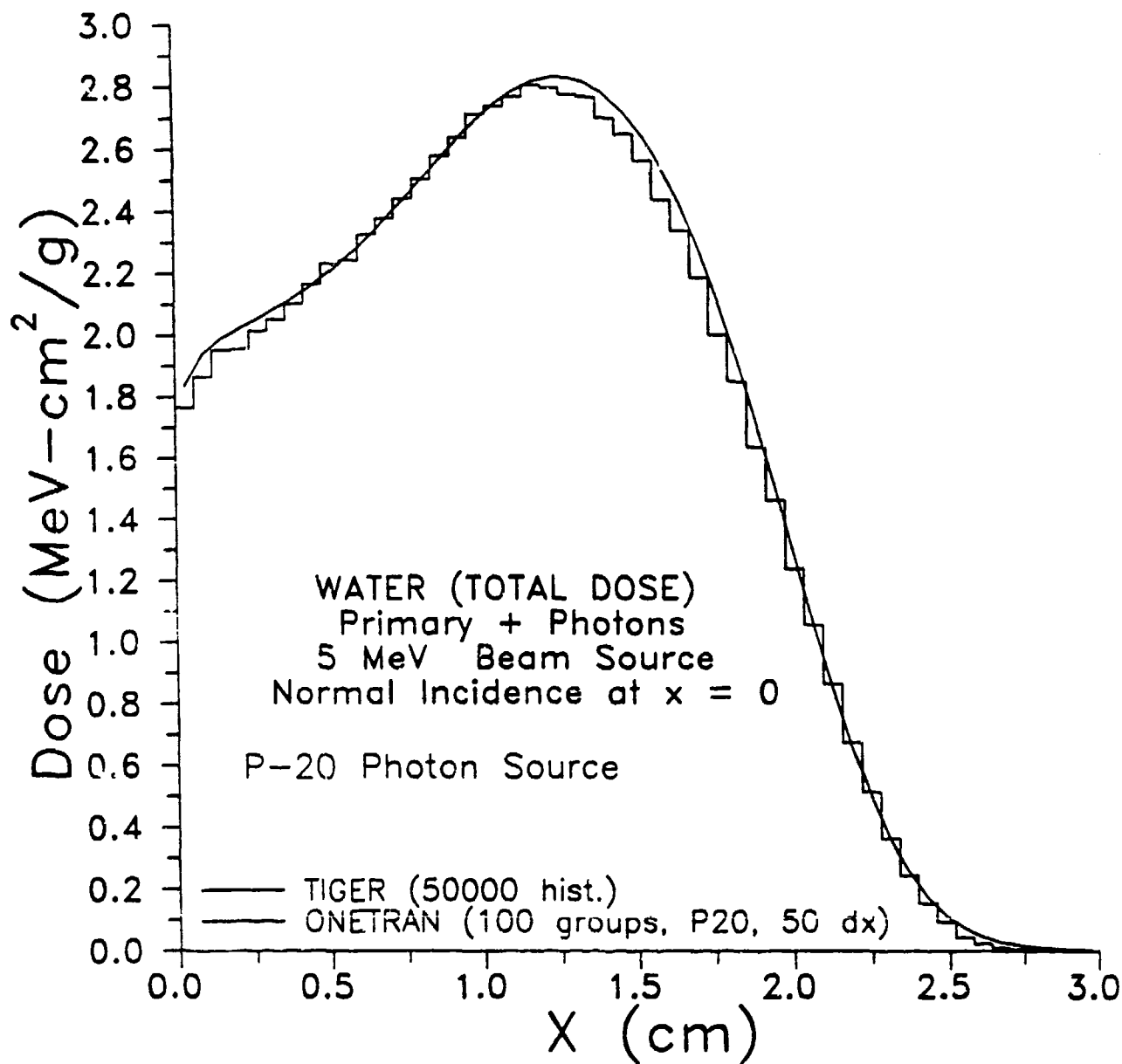
Figure 8. Energy deposition (electron + photon) profile, as calculated with ONETRAN[1] (curve) and with ITS-TIGER[2](histogram), in semi-infinite H_2O for 5 MeV electrons incident at an angle of 0°.
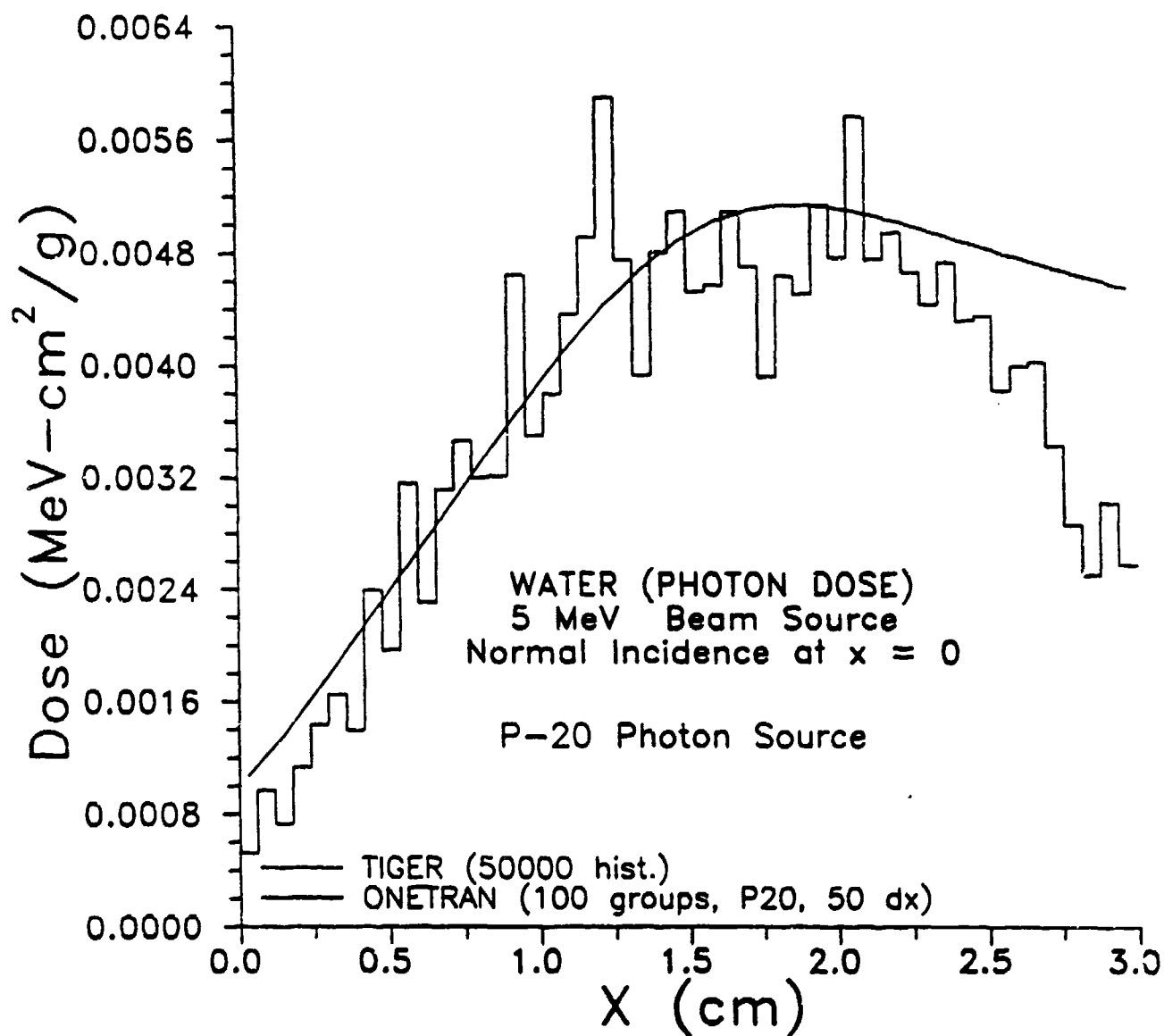
Figure 9. Energy deposition (photon) profile, as calculated with ONETRAN[1] (curve) and with ITS-TIGER[2](histogram), in semi-infinite H_2O for 5 MeV electrons incident at an angle of 0°.

In Figures 10 and 11 are plotted the total (electron + photon) and photon energy deposition profiles obtained with a 40 group coupled ONETRAN calculation for a 20 MeV electron beam normally incident on H_2O, 12 cm. thickness (20 MeV electron range in H_2O is 9.3 cm.). As in the previously described calculation, an extended scattering medium depth was assumed (60 cm.). In Figure 10 the energy deposition profile calculated with the ONETRAN code (solid curve) is compared with a TIGER Monte Carlo calculation (solid histogram) and an EGS4[7] Monte Carlo calculation (dashed histogram). The agreement between ONETRAN and TIGER is excellent to a depth of about 5.5 cm., beyond which the ONETRAN result is consistently higher. The EGS4 calculation includes knock-on electrons which account for the lower energy deposition in the first 1 to 1.5 cm. (when knock-ons are included in the TIGER calculation, the two Monte Carlo results agree very well). The photon dose results (Fig. 11) agree fairly well. We believe that the discrepancies found may be caused in part by our crude model for the photon source angular distribution. The effects of numerical straggling on the electron energy deposition profile (Fig. 10) are definitely more pronounced for the 20 MeV source than for the 5 MeV case. This was somewhat mitigated by increasing the number of energy groups, but even when we increased the number of groups to 100, the straggling effect persisted and was significant.

3.4 Knock-on Electron Production

In modelling high energy electron transport, we made modifications to our electron cross section module that would include electron energy losses and secondary electron production through knock-on collisions. As was stated, the EGS4 calculation shown in Fig.10 included the effects of knock-on electron production, while TIGER was run for the case of no knock-ons. When knock-ons were taken into account, the dose near the surface of incidence was found to be about 5 percent lower than that obtained without the knock-ons. Evidently, the highest energy electrons suffered a sufficient amount of knock-on collisions to experience significant downscatter in energy. As primary electrons penetrate the medium, the continuous slowing-down collisional and radiative energy losses outweigh any visible effect of downscatter through knock-on collisions. In order to resolve this disagreement between Monte Carlo and discrete ordinates, we installted a knock-on algorithm in the calculation of the electron energy loss cross sections for the ONETRAN calculation.

Figure 10. Energy deposition (electron + photon) profile, as calculated with ONETRAN[1] (curve) with ITS-TIGER[2](solid histogram) and EGS4[7](dashed histogram), in semi-infinite H_2O for 20 MeV electrons incident at an angle of 0°.

Figure 11. Energy deposition (photon) profile, as calculated with ONETRAN[1] (curve) and with ITS-TIGER[2] (histogram), in semi-infinite H_2O for 20 MeV electrons incident at an angle of 0°.
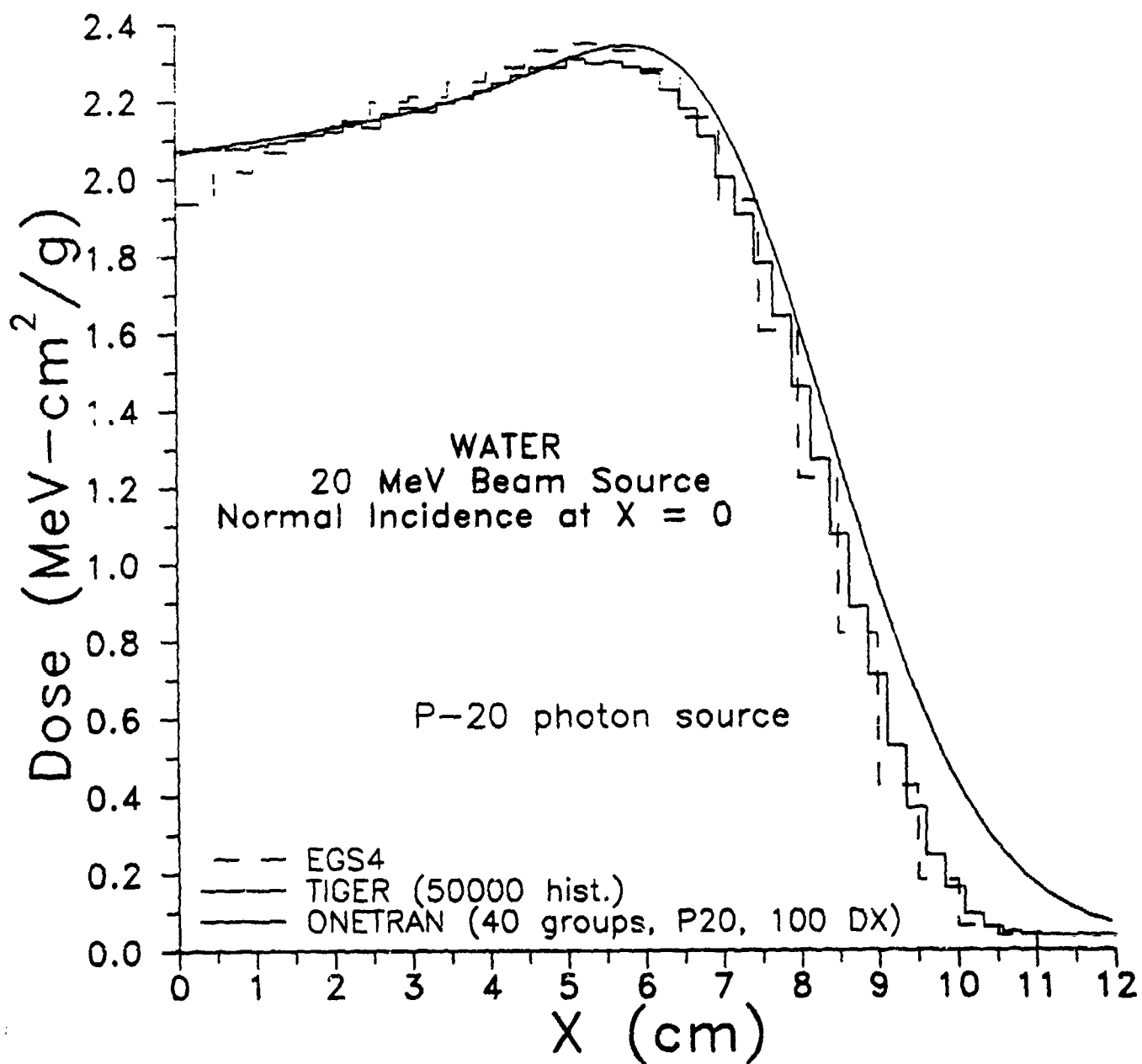
20

Accounting for downscatter of primary electrons and secondary electron production due to knock-on collisions, translated into the calculation of multigroup cross sections for these proceses. Along with this, it was found necessary to use a modified stopping power function to account for the fact that some of the energy of the primary electrons, rather than being entirely expended along the primary track, is transfered to secondary electrons, which are in turn downscattered. The definition of "restricted collision stopping power" and the means for its calculation are provided in Ref. 16.

Our calculation of the multigroup knock-on cross sections proceeded as follows: the total knock-on cross section (σ_g^{ko}) for primary electrons in group g with energy E_g is given by

$$\sigma_g^{ko} = \int_{\epsilon_c}^{\epsilon_{max}(=1/2)} \left(\frac{d\sigma}{d\epsilon}\right) d\epsilon \qquad (14)$$

where

$$\epsilon = \frac{E_{sec}}{E_g} \qquad (15)$$

and

$$\epsilon_c = \frac{E_{cut}}{E_g} . \qquad (E_{cut} \simeq 0.01 \text{ MeV}) \qquad (16)$$

E_{sec} and E_{cut} are respectively, the secondary electron energy and low energy cutoff for the secondary electrons, and[17]

$$\frac{d\sigma}{d\epsilon} = \frac{C}{\beta^2 E_g} \left\{ \frac{1}{\epsilon^2} + \frac{1}{(1-\epsilon)^2} + \left(\frac{\tau}{\tau+1}\right)^2 - \frac{(2\tau+1)}{(\tau+1)^2} \left(\frac{1}{\epsilon(1-\epsilon)}\right) \right\}, \qquad (17)$$

with $C = 2\pi N_a r_o mc^2 \left\langle \frac{Z}{A} \right\rangle$ $(=.153536 \left\langle \frac{Z}{A} \right\rangle)$, $\tau = \frac{E_g}{.5110034}$ (= the group energy in mc^2 units). β is the electron velocity divided by the speed of light, N_a = Avogadro's number, r_o = electron radius, Z and A are the atomic number and weight, respectively, and $\left\langle \frac{Z}{A} \right\rangle$ signifies the average Z/A for the molecular composition of the scattering material.

If we allow the maximum fractional energy loss of the primary to be $\epsilon_{max} = 1/2$, as indicated in the upper limit of the integral (Eq.14), then the total knock-on cross section for group g is

21

$$\sigma_g^{k o} = \frac{C}{\beta^2 E_g}\left\{ \frac{1}{\epsilon_c} \cdot \frac{1}{(1-\epsilon)} + \left(\frac{\tau}{\tau+1}\right)^2\left(\frac{1}{2}\cdot\epsilon_c\right) \cdot \frac{(2\tau+1)}{(\tau+1)^2} \ln\left(\frac{1}{\epsilon_c(1-\epsilon_c)}\right) \right\}. \tag{18}$$

In view of the above, and given the electron energy group structure, uniformly spaced energy groups of width ΔE, as depicted in Fig. 12, the cross section for and electron with energy E_g to produce a knock-on with energy $E_{g'}$ and therefore suffer a reduction in its own energy to $E_{g''}$ $(= E_g - E_{g'})$ is

$$\sigma_{g \to g',g''} = \begin{cases} \displaystyle\int_{\epsilon_1}^{\epsilon_2}\left(\frac{d\sigma}{d\epsilon}\right)d\epsilon & ; \quad (E_{g'}/ E_g < \epsilon_{max}) \\[4mm] 0 & ; \quad (E_{g'}/ E_g \geq \epsilon_{max}) \end{cases} \tag{19}$$

where

$$\epsilon_1 = \min\left\{ \frac{E_{g'}+\frac{1}{2}\Delta E}{E_g} , \epsilon_{max} \right\}, \tag{20}$$

and

$$\epsilon_2 = \max\left\{ \frac{E_{g'}-\frac{1}{2}\Delta E}{E_g} , \epsilon_{max} \right\}. \tag{21}$$

Combining Eqs. 17 ,19-21 we obtained for the group-to-group cross section,

$$\sigma_{g \to g',g''} = \frac{C}{\beta_g^2 E_g}\left\{ -\frac{E_g}{E_{g'}+\frac{1}{2}\Delta E} + \frac{E_g}{E_{g'}-\frac{1}{2}\Delta E} + \frac{E_g}{E_g-E_{g'}-\frac{1}{2}\Delta E} - \frac{E_g}{E_g-E_{g'}+\frac{1}{2}\Delta E} \right.$$

$$\left. + \left(\frac{\tau}{\tau+1}\right)^2\frac{\Delta E}{E_g} \cdot \frac{(2\tau+1)}{(\tau+1)^2} \ln\left(\left(\frac{E_{g'}+\frac{1}{2}\Delta E}{E_{g'}-\frac{1}{2}\Delta E}\right)\left(\frac{E_g-E_{g'}+\frac{1}{2}\Delta E}{E_g-E_{g'}-\frac{1}{2}\Delta E}\right) \right) \right\}. \tag{22}$$

Eq. 22 does not include the special cases where ϵ_1 or $\epsilon_2 = \epsilon_{max}$. These endpoint cases were treated in our computer program.

After a knock-on collision has occurred, the primary electron, with energy $E_{g''}$ has undergone angular deflection ω given by[18]

$$\cos\omega = \sqrt{\frac{(1-\epsilon)(\tau+2)}{2+(1-\epsilon)\tau}} . \tag{23}$$
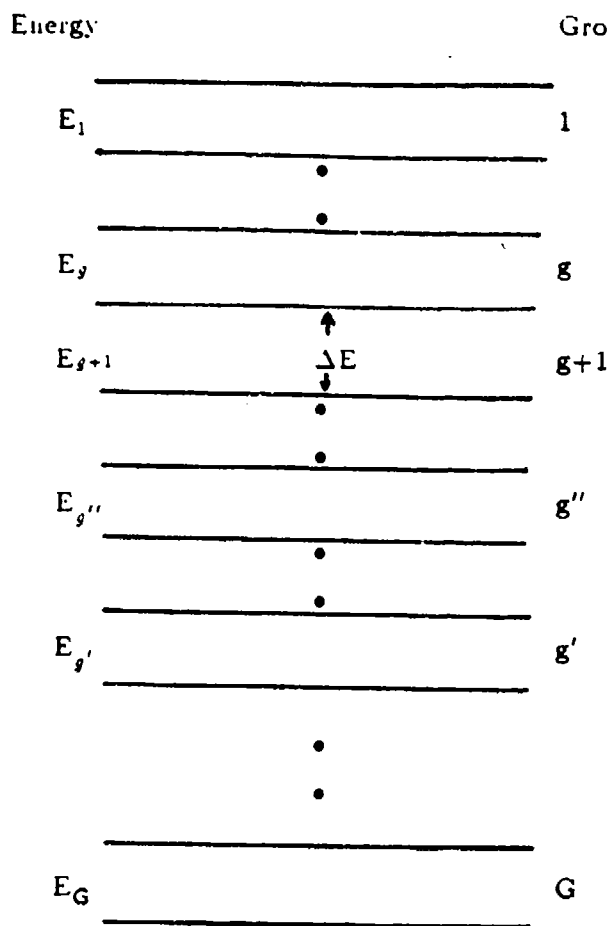
Energy   Group

Fig. 12 Electron energy group structure showing relative positions of primary and secondary electron energies

The angle χ between the knock-on secondary and the incident primary electron directions is given by[1c]

$$\cos\chi = \sqrt{\frac{\epsilon(\tau+2)}{2 + \epsilon\tau}} \quad . \qquad (24)$$

The Legendre coefficients of the angular deflection dependence of the primary electron downscatter cross section $\sigma_{g \to g''}$ are then given by

$$\sigma_l^{g \to g''} = \sigma_{g \to g',g''} P_l(\cos-) \ . \qquad (25)$$

The corresponding Legendre coefficients for the direction of the secondary electron are

$$\sigma_l^{g \to g'} = \sigma_{g \to g',g''} P_l(\cos\chi) \ . \qquad (23)$$

With some experimentation, we found that ϵ_{max} could be adjusted to impose realistic limits on the primary electron energy loss due to knock-on collisions. While the theoretical value for $\epsilon_{max} = 1/2$, stepwise examination of the integrated values of Eq.17 revealed that such occurrences were rare. The best agreement with Monte Carlo was obtained with the following upper limits on the knock-on electron energy: for primary energy 5 MeV and above, $E_{sec}^{max} = 2$ MeV; for primary energies below 5MeV, $E_{sec}^{max} = 200$ keV. To account for the energy carried off by the secondary electrons, a separate transport calculation for the knock-ons was performed. Figure 13 shows the total energy deposition profile, obtained using the knock-on algorithm, for the 20 MeV beam source on H_2O. Even though agreement with the EGS4 result is much improved in the first 1.5 cm. over that shown in Fig. 10, this calculation, also in contrast to the Fig. 10 curve, consistently underestimates the dose in the region beyond the profile maximum. It is clear, from the above results, that improvement in both the knock-on algorithm and the energy discretization s.... .ie is required.

Figure 13. Energy deposition (electron + photon) profile, as calculated with ONETRAN[1] (curve) with ITS-TIGER[2](solid histogram) and EGS4[7](dashed histogram), in semi-infinite H₂O for 20 MeV electrons incident at an angle of 0°. The knock-on electron contribution is included in this calculation.
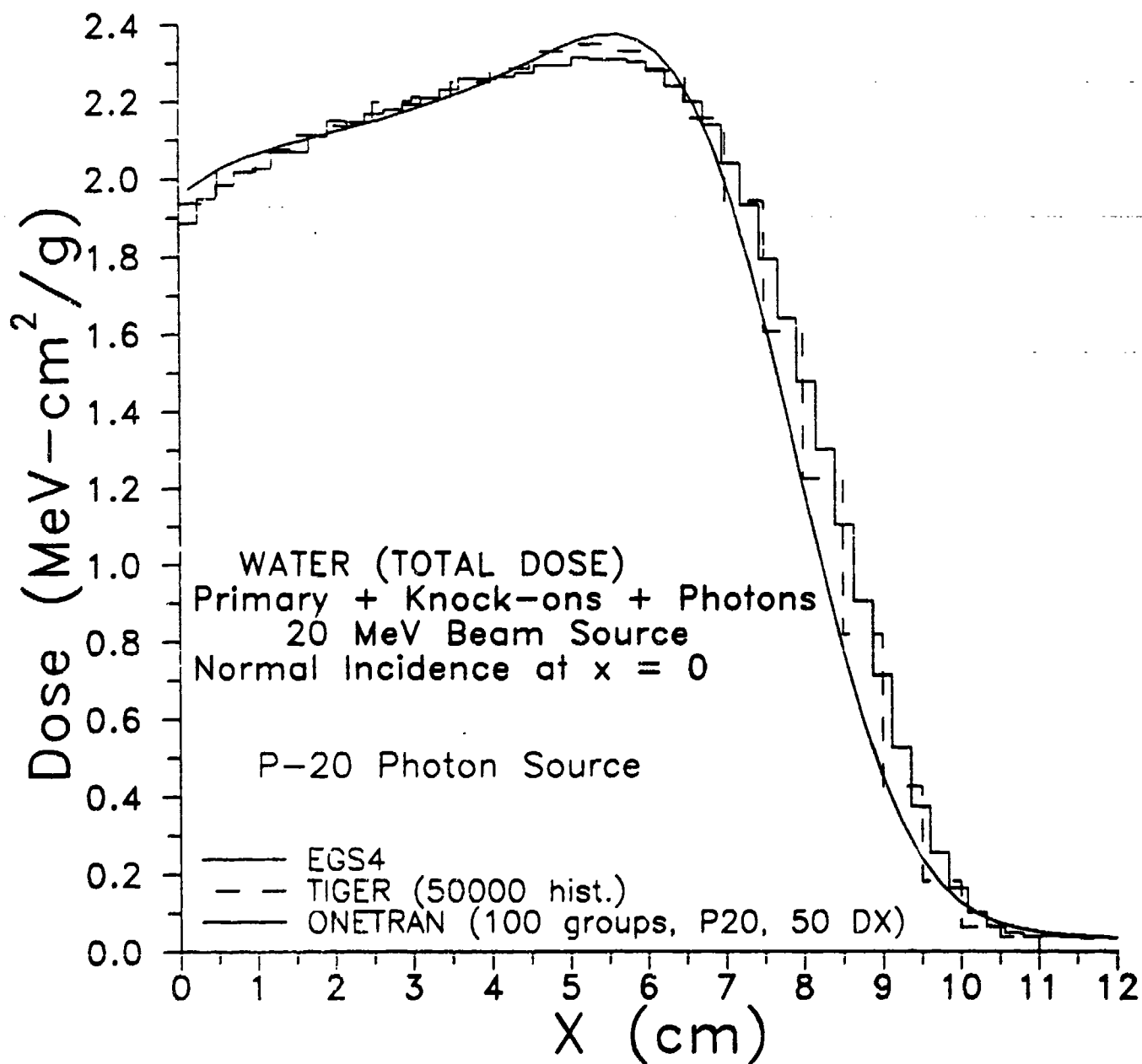
24

3.5 Structure of the Coupled Electron-Photon Discrete Ordinates Programs

We wrote and/or modified programs for the one-dimensional coupled electron-photon discrete ordinates calculation with a modular design consisting of four sections:

1) an interactive (with the user) program to collect the user-specified information which defines the problem to be run and translates this information into an input data file formatted to be compatible with the cross section and transport codes.

2) cross section generation programs which are modified versions of DATPAC[2] (for electrons) and GAMLEG[14](for photons).

3) data handling programs to couple the electron and photon transport calculations by converting and passing data between them; compute quantities such as energy deposition profiles, energy and angle spectra; prepare plot data files.

4) ONETRAN[1] transport code.

Of the above, the programs in the second and fourth categories are well documented by their originators. The linking programs, third category, perform perfunctory programming tasks. The first program, the user-calculation interface, which is run interactively, has self-explanatory prompts, and the input format from the keyboard is free form. We wrote two versions of this program, one in BASIC and one in FORTRAN-77, so that it can be run either on an IBM PC or compatible (BASIC version) or on a mainframe such as VAX or MicroVAX. The user is interrogated regarding such problem-defining items as the number of mat als in the scattering medium; the chemical composition (element symbol and weight f.ac   a. of each material; source type (electron, photon, angular distribution, spatial distrubu a. en   spectrum); whether a photon transport calculation is to be run; whether a knock-on c .culation is to be included; etc. This program also creates the list of files (with definitions and names linked in a directory) to serve as repositories for data (such as electron and photon fluxes, cross sections, plot data). These files are used by the data handling programs (category 3, above) and ONETRAN. This program also contains provisions for eliminating redundant calculations of cross section sets by providing the user with the opportunity to specify the names of already existing cross section files which may be pertinent to the problem to be run. A run of this program results in the creation of an "input run deck" for the transport calculation on the mainframe. If the BASIC version is used, the "run deck" file is written to a floppy diskette which can then be transferred to the mainframe for a batch mode transport calculation. A hard copy of the prompts, responses, run file and a data file directory is printed.

25

III. ELECTRON TRANSPORT CALCULATIONS IN ONE-, TWO- AND THREE DIMENSIONS

1. Introduction

During this reporting period, there were many opportunities to provide benchmark electron transport calculations for the purposes of testing newly developed one- and two-dimension electron transport techniques and scattering cross section formulations. Most of the benchmark calculations were made using the Monte Carlo method. In addition to performing benchmark Monte Carlo and S_n calculations in one-dimension[19], we also wrote a new single collision, electron Monte Carlo (1-d) transport code[21]for the purpose of testing the effectiveness of a new scattering cross section, the "smart" cross section.

Our participation in research in the area of two-dimensional electron transport calculation methods consisted of providing benchmark Monte Carlo calculations, using the ITS[2] Series ACCEPT code, for two papers. The first[22]demonstrated the feasibility of using the "smart" cross section in conjunction with first collision (or once-scattered) sources for electron beam S_n calculations. The second of these[23]represents a continuation of the electron beam source work. It contains, however, a more extensive set of comparisons between S_n and Monte Carlo results consisting of isodose contour maps and energy deposition profiles in one-dimension across the two-dimensional scattering medium.

We conclude this chapter with a discussion of three-dimensional electron transport calculations. A recent paper[24] which reports the results of a set of S_n and Monte Carlo calculations of energy deposition in and electron exit currents from realistic microelectronic device geometries due to the incidence of a beam of electrons. We provided the device geometry description and mock-up as well as the Monte Carlo calculations for this paper.

2. Monte Carlo and S_n Calculations of Electron Transport in One-Dimension for Validation of the Method of Streaming Rays

In a paper which appeared in 1987[19], a complete description was given of the application of the method of streaming rays to one-dimensional electron transport problems. Earlier papers (*op. cit.*) had already demonstrated the applicability of this calculation method to neutral particle transport in two-dimensional media with void regions and time-dependent one-dimensional problems. The similarity between the time-dependent neutral particle transport

equation and the Spencer-Lewis equation for electron transport strongly suggested the applicability of the streaming ray (SR) method to this problem. In the Spencer-Lewis equation, the electron energy is the continuous-slowing-down-approximation (CSDA) defines a unique relationship between the electron pathlength and stopping power. The reason for employing this approximation is that the major mechanism for electron energy loss, inelastic collisions with other electrons, cannot be treated in a tractable way by a form of the transport equation that considers one collision at a time. There are far too many of these collisions, and the electron energy loss resulting from an individual inelastic collision is miniscule. The SR method is highly compatible with CSDA because the SR model assumes that the motion of an electron is assumed to take place along a streaming ray (a characteristic line of the Spencer-Lewis equation). With the SR method the electron pathlength/energy increases/decreases continuously. This is the basic point of departure from the conventional multigroup S_n method in which the spatial dependence of the Spencer-Lewis equation solution is obtained by finite differencing over a series of discrete steps for a given constant energy value. When, by means of an iterative spatial differencing scheme, the equation is balanced for a particular energy group, the electron energy is then decremented by a discrete step to the next lower(in energy) group.

Numerical errors associated with the spatial and energy discretization of the S_n method give rise to artificial straggling. In some cases this leads to a fortuitously close agreement with Monte Carlo and experimental measurements of energy deposition because the Monte Carlo method is capable of accounting for the actual physical straggling, the departure from CSDA. Numerical straggling in the S_n method introduces large errors in the calculated electron energy spectra unless a very large number of energy groups is used. This effect is greatly reduced with the SR method. Ref. 19 provides a method for simulating physical straggling in addition to CSDA in the transport calculation. Fig. 14 shows a comparison of energy deposition results obtained with the SR, S_n[1] and Monte Carlo[2] methods. These results were obtained for the case of a slant source (μ_0 = .916667 , see Fig. 14 inset) of 0.2 MeV electrons on a 0.04 g/cm^2 Al slab. The SR calculation was formulated and performed by Filippone, while the S_n and Monte Carlo calculations were done by Woolf. As can be seen, the SR calculation, which has straggling effects included, agrees better with the Monte Carlo benchmark than either of the 2 S_n calculations.
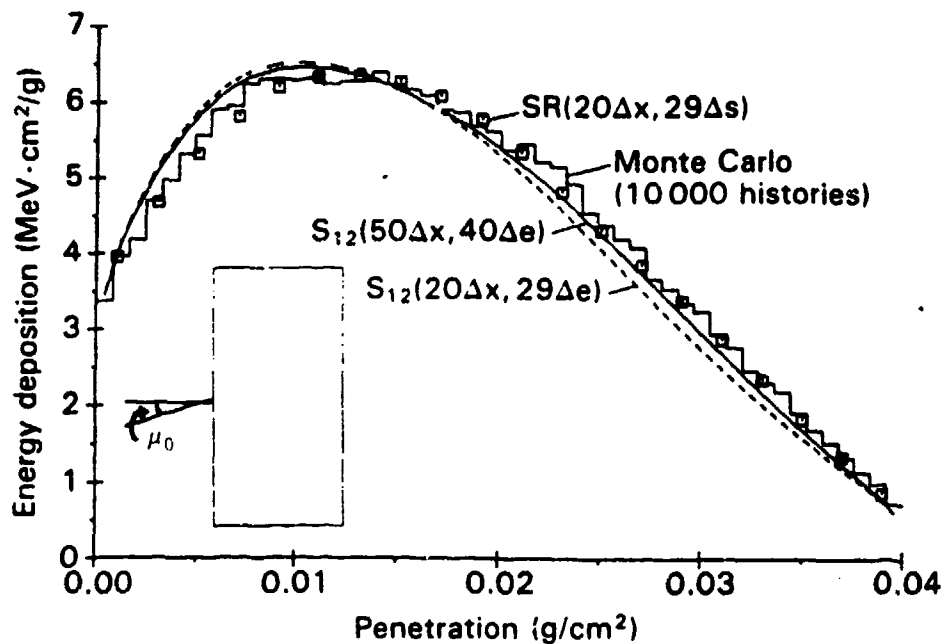
27

Figure 14. Energy deposition profile for 0.2 MeV electrons obliquely incident ($\mu_0 = 0.916667$) on a 0.04 g/cm^2 thick Al slab (Ref. 19).

Figure 15. CSDA transmission spectra, as calculated by the SR, Monte Carlo and S_n methods, for 0.2 MeV electrons obliquely incident ($\mu_0 = 0.916667$) on a 0.04 g/cm^2 thick Al slab (Ref. 19).

28

Fig. 15 shows the CSDA transmission spectra for the same 0.2 MeV source geometry. However in both the SR and Monte Carlo calculations. CSDA was assumed (that is, the straggling effects were omitted on purpose). The "countershove" correction, referred to in the figure, is a method devised by Filippone to correct the spatial discretization errors associated with cell-collided electrons. SR treats the collided and uncollided portions of the electron flux separately. The uncollided part is treated exactly, while the collided part, generally much smaller if, for example, extended transport corrected cross sections are used, is treated in the same manner as in S_n. As can be seen from Fig. 15, the SR and Monte Carlo results agaree very well, while even the 80 group S_n calculation is far off the mark above 0.13 MeV. The delta function referred to in the figure occurs at the maximum energy at which the uncollided electrons can emerge from the slab. given the slant path and CSDA. Fig. 16 compares the SR and Monte Carlo benchmark calculations with the inclusion of physical straggling. Again the agreement between the two methods is good.
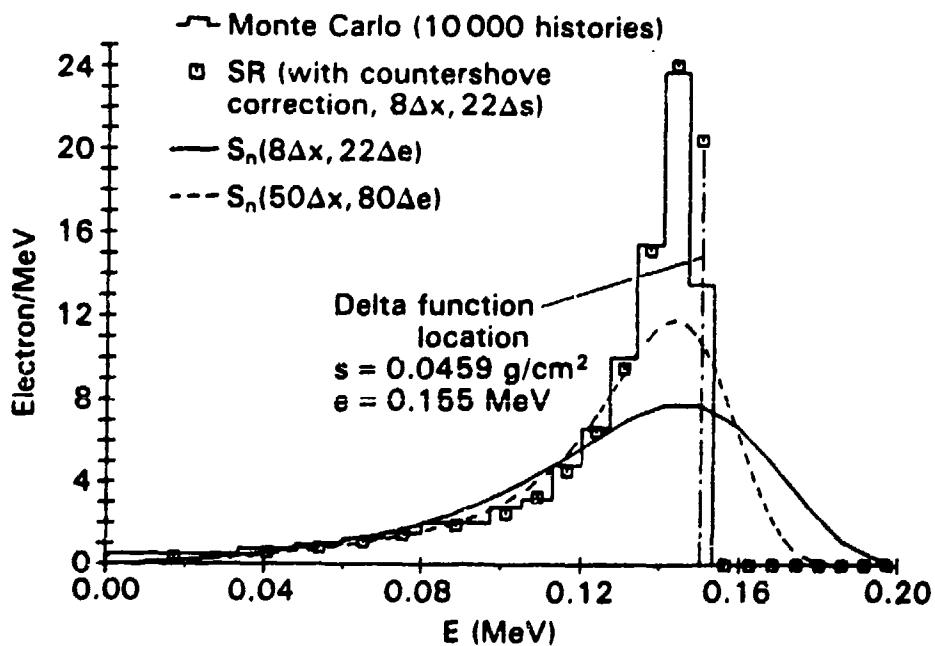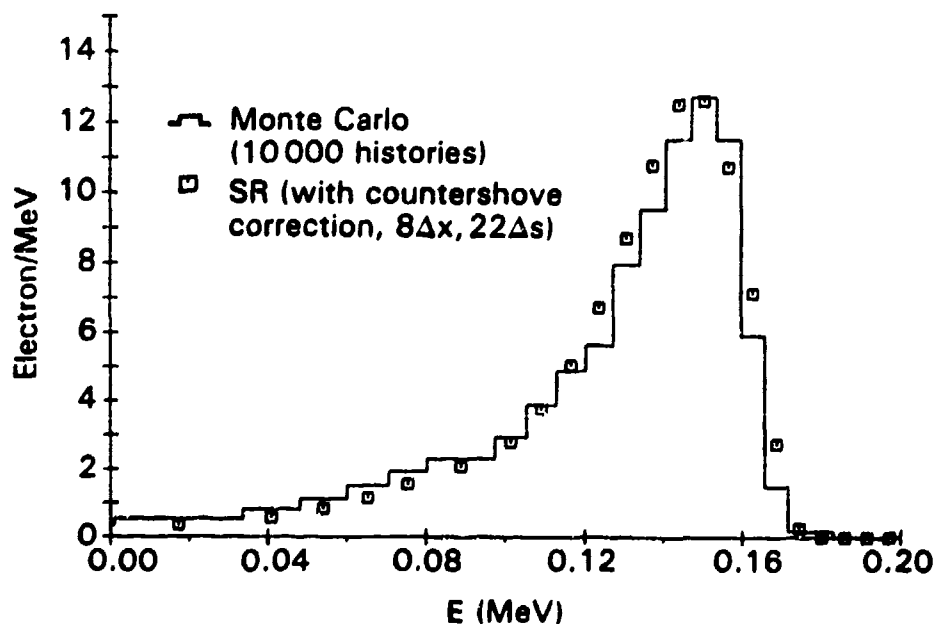

Figure 16. Transmission spectra, as calculated by the SR and Monte Carlo methods, for 0.2 MeV electrons obliquely incident ($\mu_0 = 0.916667$) on a 0.04 g/cm^2 thick Al slab. Straggling effects are included in both calculations (Ref. 19).

3. Implementation of SMART[20] Scattering Theory in One-Dimensional Monte Carlo Electron Transport Calculations[21]

The SMART[20] scattering cross section, originated by Filippone, is a representation of an angular redistribution function for electron scattering based on Goudsmit-Saunderson theory (see Ref. 20). The Goudsmit-Saunderson multiple scattering theory allows one to obtain infinite medium solutions for the Spencer-Lewis equation. The basis of SMART scattering theory is the conjecture that the validity of the scattering theory, and its representation through the scattering matrix should not depend on the problem geometry. A rigorous treatment of SMART scattering theory is given in Ref. 20, thus it is not necessary or appropriate to repeat it here. As a result of collaboration between Drs. Filppone (Univ. of Arizona) and Woolf (Arcon Corp.) a paper was written and published, first in a meeting proceedings[21a], and then in *Nuclear Science and Engineering*[21b] describing the implementation of this cross section, in scattering matrix form, in a Monte Carlo electron transport code written by Dr. Woolf. The term "SMART" is a acronym for simulating many accumulative Rutherford trajectories. These scattering matrices were originally developed for implementation with the discrete ordinates (S_n) method. One of the purposes of performing these Monte carlo calculations was to demonstrate that the validity of the SMART scattering theory did not depend on the method of implementation; that its applicability to the S_n method was not due to a numerical artifact of the method. The other purpose of this work was to introduce a possible alternative means for performing electron Monte Carlo calculations to the implementation of multiple scattering theory as manifested in the ITS code series[2]. It was felt that application of SMART scattering theory in the Monte carlo method could result in a more economical means for performing these calculations than those which presently exist. This is due in large part to the fact that an essential characteristic of this theory is a large effective mean free path for electrons, much large than the true single collision mean free path. The extent to which this feature would result in a more economical calculation than that afforded by, say, the TIGER[2] code, which employs a multiple collision cross section and is also much more economical than true single collision Monte Carlo, remained to be determined by the results of this paper.

The Monte Carlo code written for the implementation of the SMART scattering theory, incorporated a single collision trajectory analog algorithm. It departed from conventional Monte Carlo algorithms in two important ways: 1) the calculation of the intercollision distance

takes into account the variation of the total cross section with electron path length and direction: and 2) the direction cosines of the electron trajectory after a collision has occurred are obtained directly from the scattering matrix. The total electron trajectory path length, determined from the electron CSDA range, was divided into a number of equal path length steps Δs. The intercollision path length was determined by sampling the well-known exponential attenuation laws. When, along the intercollision parth segment, a given Δs step was traversed, the total cross section, a function of path length and direction, was updated.

The presently existing form of the Monte Carlo code treated one-dimensional slab geometry problems. Extension to two- and three-dimensions would be straightforward. For purposes of testing the code, two 200 keV electron source configurations, beam and isotropic, were assumed to be incident on two thicknesses of Al , .01 g/gm^2 and .02g/cm^2. The incident obliquity of the beam source was defined by its cosine $\mu_0 = 0.916667$. The results obtained with this code, emergent energy spectra and energy deposition profiles, were compared with benchmark runs of TIGER[2]. A sampling of the results given in the paper are shown in Figs. 17-20. A comparison of the transmission spectra (SMART and TIGER) through 0.01 g/cm^2 Al is shown in Figs. 17 and 18 for the beam and isotropic sources, respectively. Beam source reflection spectra for the thicker slab are compared in Fig. 19. Finally, the energy deposition profiles for the beam source in .02 g/cm^2 are compared in Fig. 20. As can be seen, the results obtained with the SMART Monte Carlo calculation compare very well with the TIGER benchmarks. Both codes were run with 10000 electron case histories. In all cases tested. it was found that the SMART matrix Monte Carlo calculations ran approximately 3 times faster than TIGER. Since our code was developed for research rather than production purposes, it is likely that this run time ratio could be improved.

31

Figure 17. Transmission spectrum for a 0.2 MeV electron beam source, with incident obliquity $\mu_0 = 0.916667$, incident on a 0.01 g/cm^2 Al slab, as calculated by SMART cross-section Monte Carlo and ITS-TIGER[2] Monte Carlo (Ref. 21).
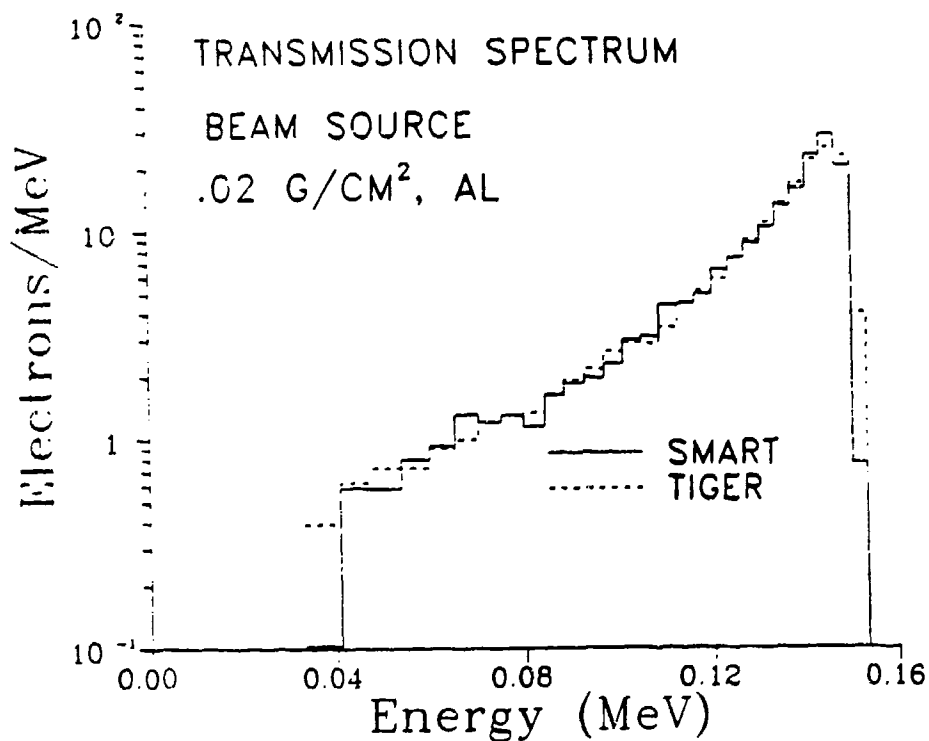
Figure 18. Transmission spectrum for a 0.2 MeV electron beam source, with incident obliquity $\mu_0 = 0.916667$, incident on a 0.02 g/cm^2 Al slab, as calculated by SMART cross-section Monte Carlo and ITS-TIGER[2] Monte Carlo (Ref. 21).

32

Figure 19. Reflection spectrum for a 0.2 MeV electron beam source, with incident obliquity μ_c = 0.916667, incident on a 0.02 g/cm^2 Al slab, as calculated by SMART cross-section Monte Carlo and ITS-TIGER[2] Monte Carlo (Ref. 21).

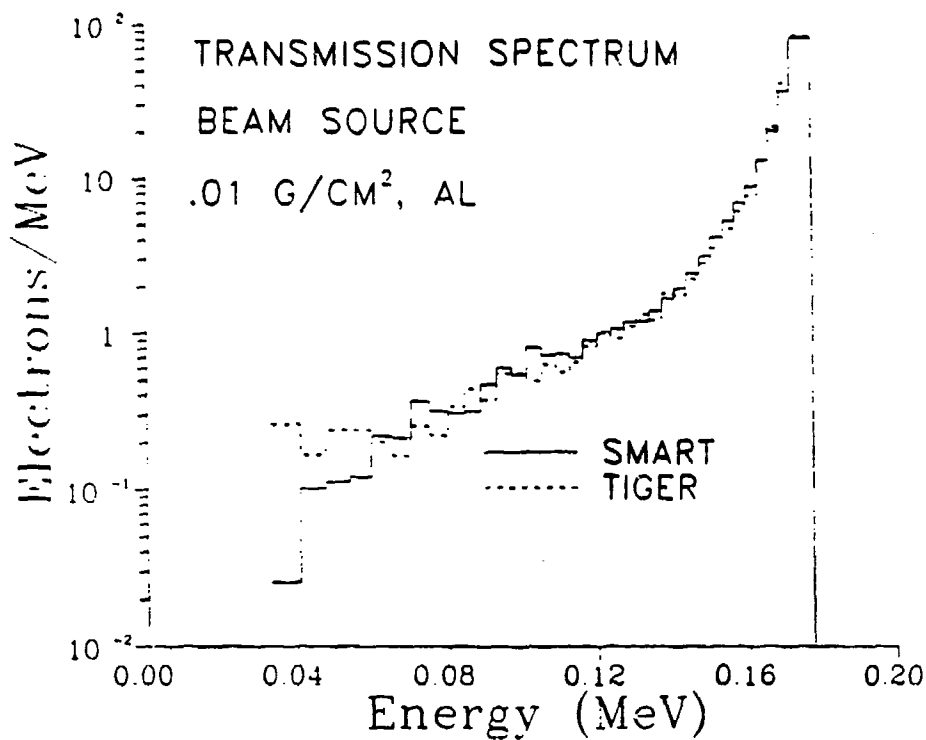Figure 20. Energy deposition profile for a 0.2 MeV electron beam source, with incident obliquity μ_0 = 0.916667, incident on a 0.02 g/cm^2 Al slab, as calculated by SMART cross-section Monte Carlo and ITS-TIGER[2] Monte Carlo (Ref. 21).
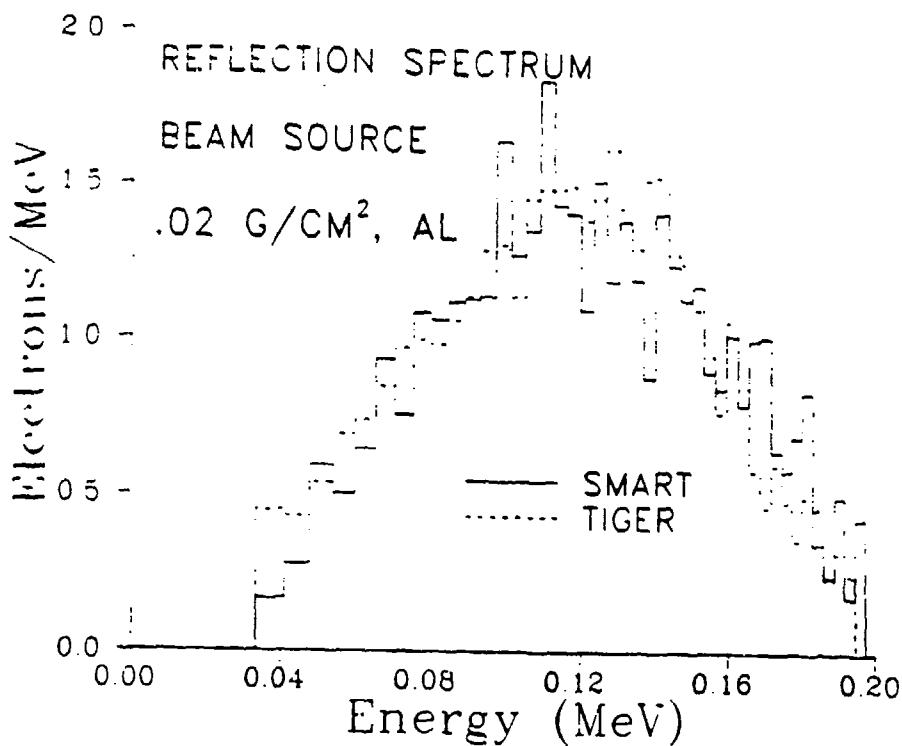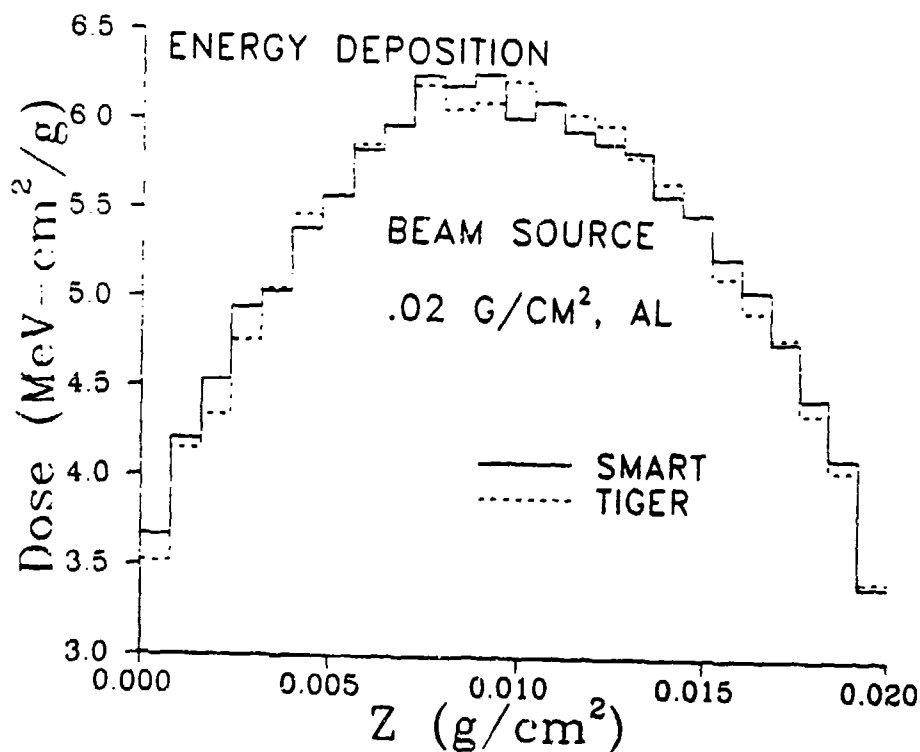
33

4. Electron Transport Calculations in Two-Dimensions[22,23]

4.1 Determination of Dose Profiles and Isodose Contours for 200 keV Electron Transport in Two-Dimensions

In a paper that resulted from a collaboration among W. L. Filippone, S. Woolf and J.C. Garth[22], it was reported that the Spencer-Lewis equation for electron transport in two-dimensions was solved using the S_n method with diamond differencing in the spatial and pathlength variables. Dose profile calculations in two-dimensions were made for 200 keV electrons incident on Al. The electron source configuration were of three types: 1) normally incident beam; 2) beam with slant incidence (45°); and 3) isotropic incidence. Comparison runs were also made with the ACCEPT[2] Monte Carlo code.

In two-dimensions, the Spencer-Lewis equation for the electron flux $\phi(x,y,s,\Omega)$ is given by[22]

$$\left(\frac{\partial}{\partial s} + \Omega_x\frac{\partial}{\partial x} + \Omega_y\frac{\partial}{\partial y} + \sigma(s)\right)\phi(x,y,s,\Omega) = \int_{4\pi} d\Omega'\sigma(s,\Omega'\rightarrow\Omega)\phi(x,y,s,\Omega') + Q(x,y,s,\Omega) , \qquad (24)$$

where Ω_x, Ω_y = the x and y velocity direction cosines,

  s = electron pathlength,

  $\sigma(s)$ = total scattering cross section.

  $\sigma(s,\Omega'\rightarrow\Omega)$ = differential scatering cross section,

and $Q(x,y,s,\Omega)$ = electron source density.

The energy deposition function, W(x,y), is determined from the Spencer-Lewis solution $\phi(x,y,s,\Omega)$ as follows:

$$W(x,y) = \int |\frac{dE}{ds}|\phi(x,y,s)\ ds, \qquad (25)$$

where

$|\frac{dE}{ds}|$ is the electron stopping power, and $\phi(x,y,s)$ is the scalar flux.

Eq. 24 is solved using the S_n method with diamond differencing. The solution steps are outlined in Ref. 22. Because of the extreme anisotropy of the electron scattering kernel, SMART[20] scattering theory was employed to render the S_n numerical solution feasible. An effective scattering matrix was defined in order that the required number of discrete ordinates

34

for the description of the angular redistribution of electrons would not exceed manageable limits. Figures 21 and 22 are isodose contour plots of the energy deposition in Al for normal and 45° electron beams, respectively. In both cases, the dimensions of the Al rectangle were 0.01 x 0.02 g/cm^2. For a direct quantitative comparison with the Monte Carlo method. we ran the ACCEPT[2] code, which is a three-dimensional electron Monte Carlo program, for the two cases shown in Figs. 21 and 22. The two-dimensional problem geometry was simulated by extending the z-coordinate of the scattering medium to essentially $\pm\infty$, where "∞" is taken to be $\sim$1.5 electron range units. Figures 23 and 24 show comparisons of dose profiles obtained with S_n calculations and ACCEPT. These profiles are the integrated (over area) doses across the rows A. B. and C as indicated in the accompanying cell diagram. In Fig. 23. the isotropic source results for two S_n calculations, S_6 and S_{12}, are compared with Monte Carlo, while in Fig. 24, the corresponding comparisons for the normal beam source results for S_4 and S_6 is are shown. As can be seen, overall agreement between our Monte Carlo calculations and Filippone's S_n calculations is very good.
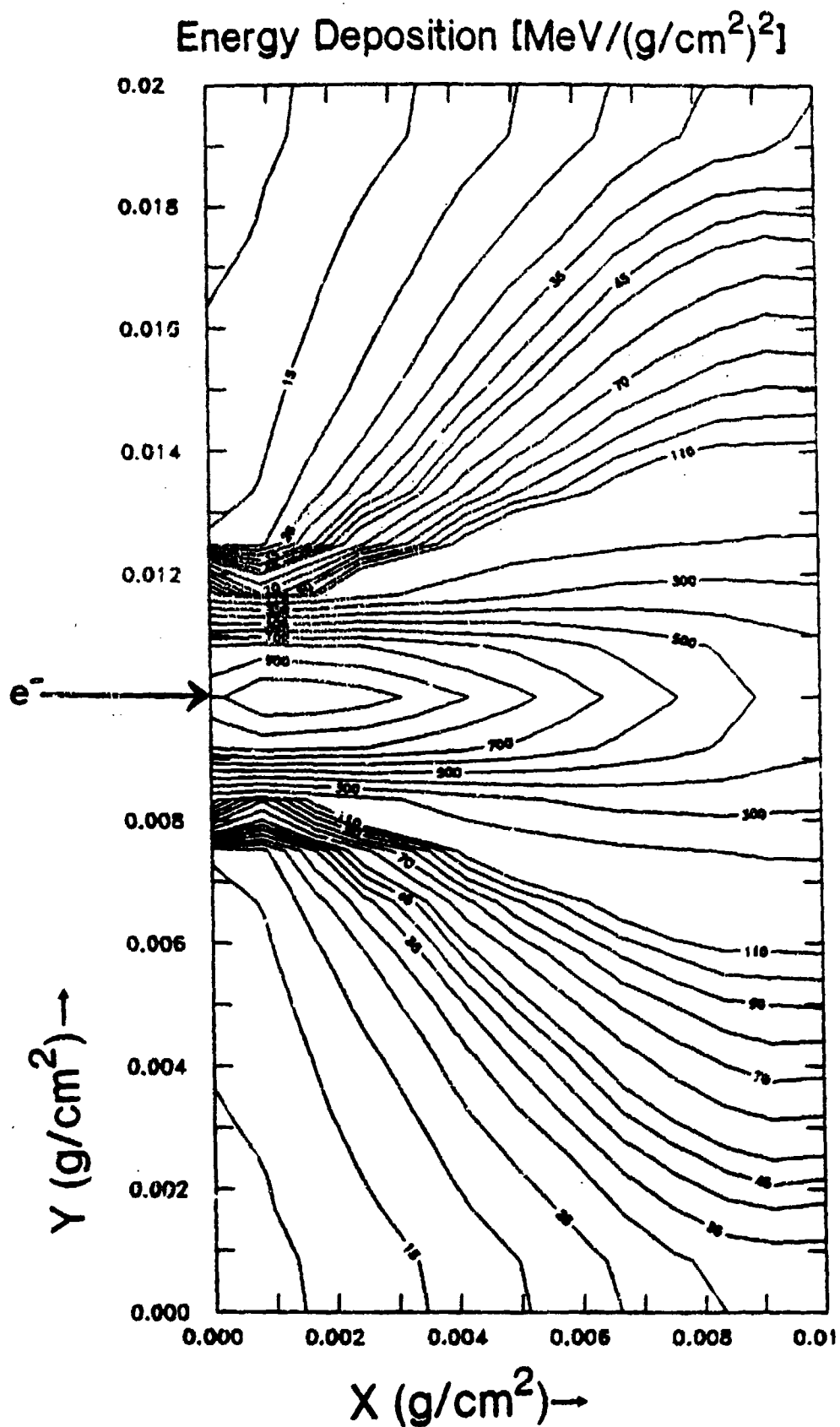
Figure 21. Energy deposition (isodose) contour plots for a 0.2 MeV electron beam normally incident on Al rectangle of dimension 0.02 g/cm² x 0.01 g/cm² (Ref. 22).

Energy Deposition [MeV/(g/cm^2)^2]
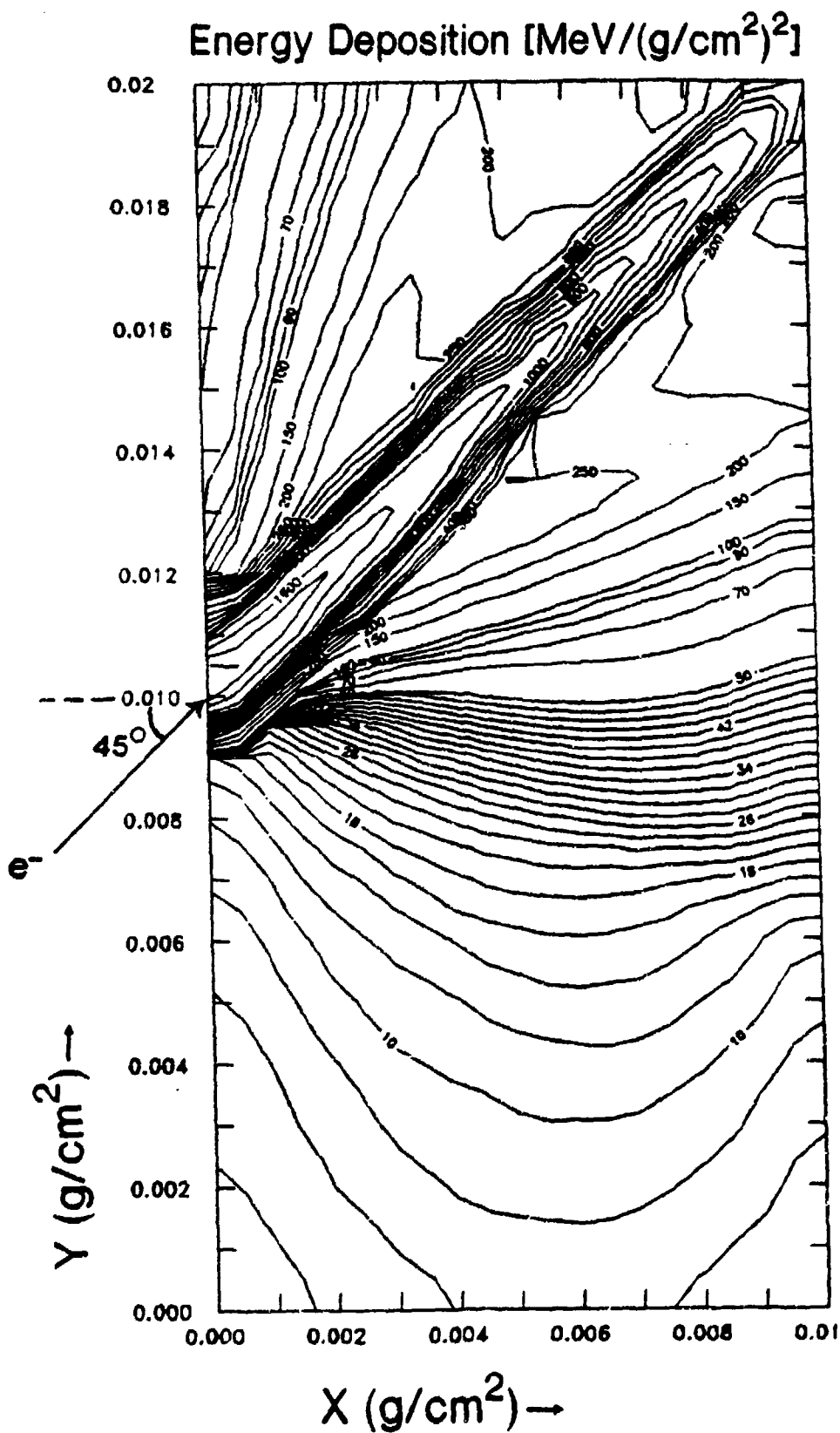
Figure 22. Energy deposition (isodose) contour plots for a 0.2 MeV electron beam incident at a 45° angle on Al rectangle of dimension 0.02 g/cm^2 x 0.01 g/cm^2 (Ref. 22).

Figure 24.Comparison of S_n and Monte Carlo (ITS-ACCEPT[2]) dose profiles for a 0.2 MeV electron beam source normally incident on Al rectangle of dimension 0.02 g/cm^2 x 0.01 g/cm^2. The locations of rows A, B and C are shown in the accompanying diagram accompanying Fig. 23 (Ref. 22).

Figure 23.Comparison of S_n and Monte Carlo (ITS-ACCEPT[2]) dose profiles for a 0.2 MeV isotropic electron source incident on Al rectangle of dimension 0.02 g/cm^2 x 0.01 g/cm^2. The locations of rows A, B and C are shown in the diagram (Ref. 22).

38

4.2 Two-Dimensional Electron Transport Calculations with Once-Collided Beam Sources

In a continuing collaboration among W.L. Filippone, S. Woolf and J.C. Garth on two-dimensional electron transport problems, a paper[23] was presented at the November, 1987 meeting of the American Nuclear Society in which the use of analytic first collision (or once-collided) electron sources was introduced into two-dimensional S_n electron transport calculations. In previous one-dimensional electron transport calculations, it was found that S_n calculations could not be done for beam sources unless an analytically derived once-scattered source was used. Th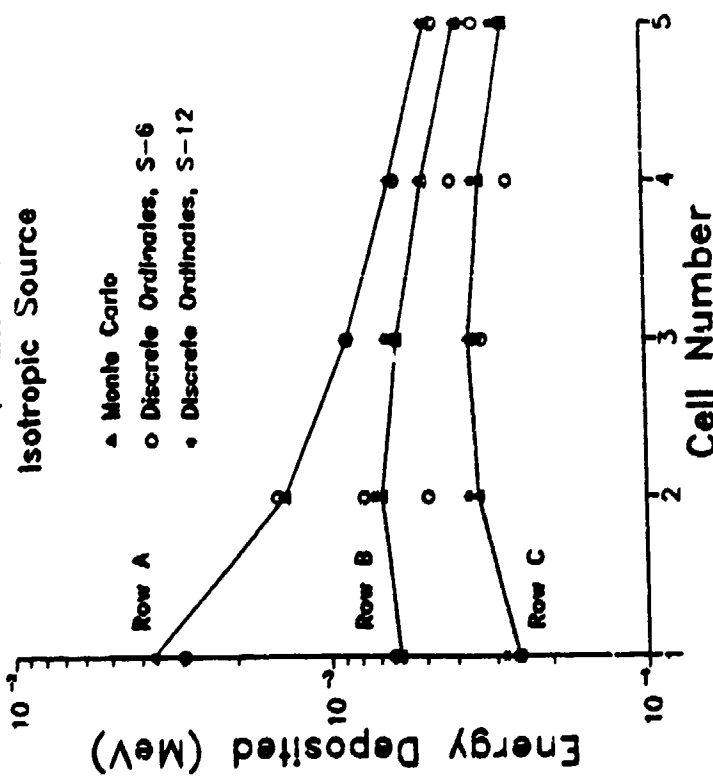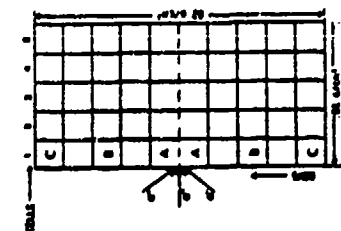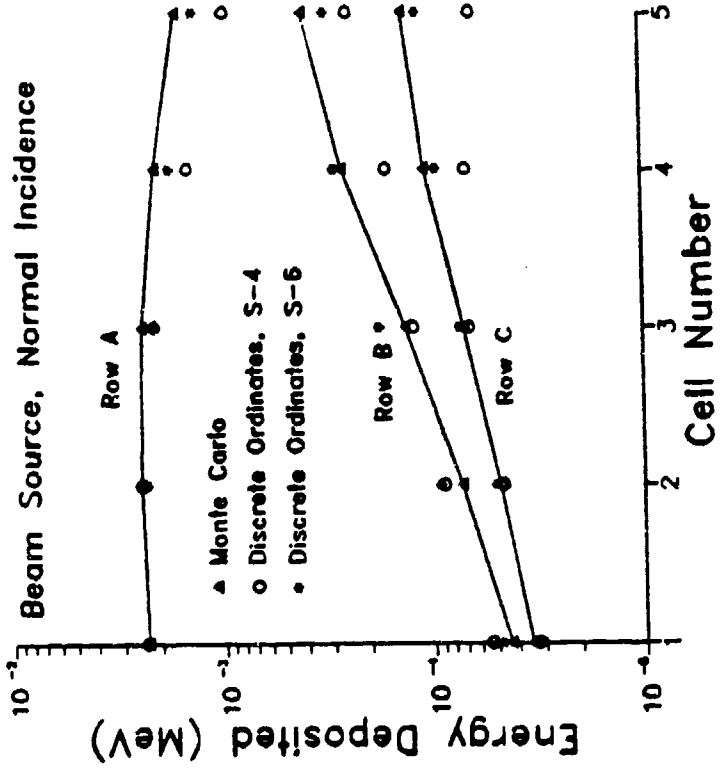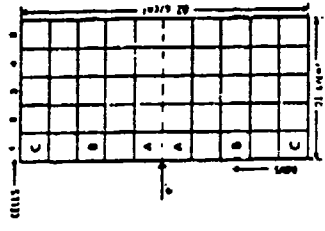is was due to the high degree of anisotropy associated with electron scattering kernels. While in two-dimensional electron transport S_n calculations incorporating the SMART cross section, this anisotropy could be handled without the aid of the once-scattered source[22], it was believed that use of such a device, in conjunction with the SMART cross section, could greatly improve the accuracy of these calculations. As in the paper discussed in section 4.1, we provided the Monte Carlo benchmark calculation for this work. A 200 keV beam of electrons was assumed incident on an Al slab of dimension .01 g/cm^2 x .02 g/cm^2. The angle of incidence in the x-y plane was 45°, and the point of incidence was located at x=0, y=.01, as shown on the inset of Fig. 25. Also shown in Fig. 25 are the two energy deposition results, S_n (S_4) and Monte Carlo (ACCEPT[2], 100000 case histories). To aid in the interpretation of the diagrams of Fig. 25, it should be pointed out here that the rectangular slab was divided into 50 square zones (.002 x .002), and the histograms display the energy (keV) deposited in each zone. The results appear to agree well. The advantage in computation speed of S_n over Monte Carlo became especially apparent in this work. It was found that the S_4 calculation consumed ~1/30-th as much computer time as did the Monte Carlo.
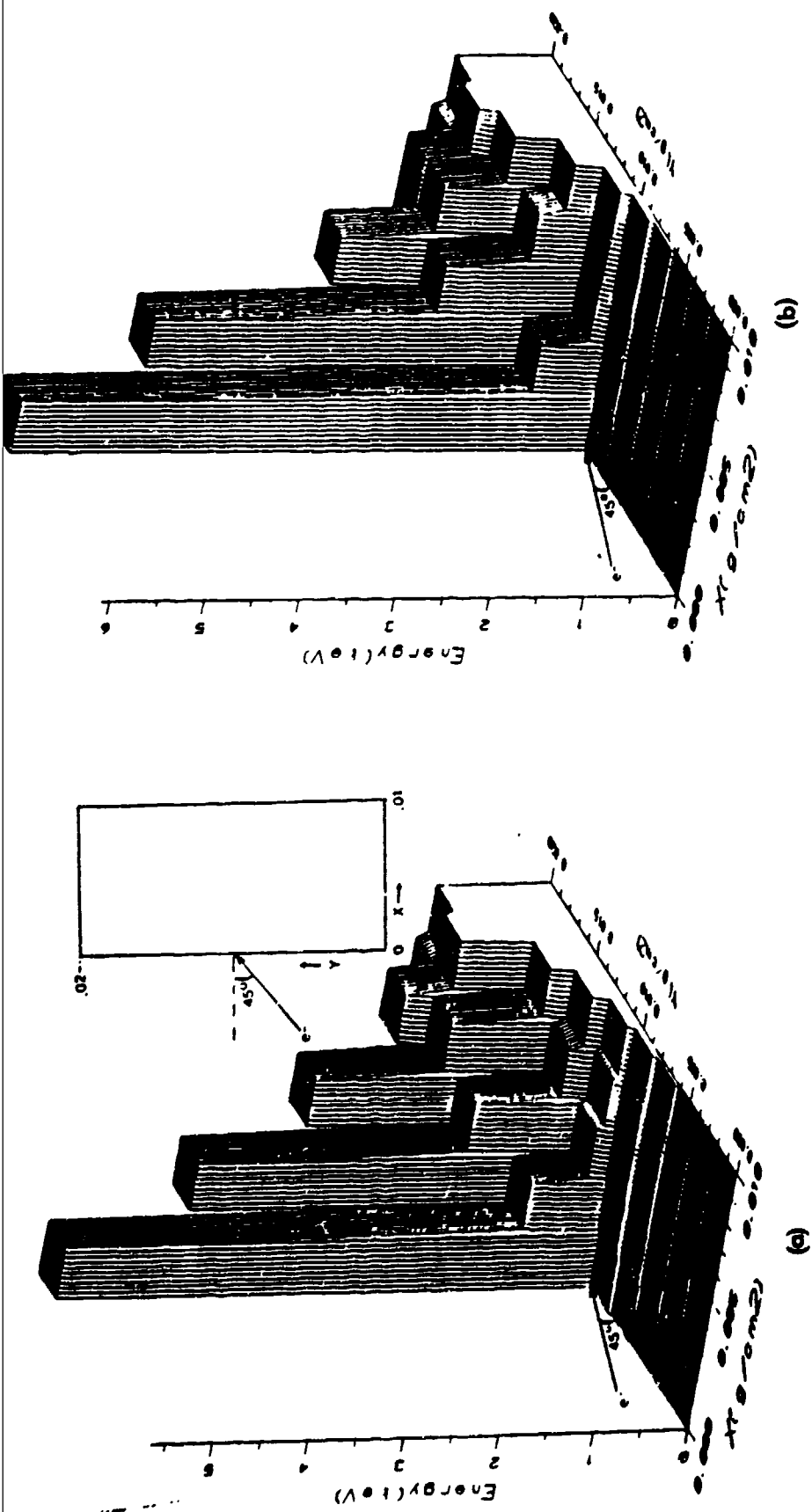
Figure 25. Energy deposition in a rectangular Al slab of dimension 0.01×0.02 g/cm^2 resulting from a 45° slant beam of 0.2 MeV electrons incident at $x=0.0$, $y=0.01$: (a) discrete ordinates S_4 calculation; (b) ITS-ACCEPT[2] Monte Carlo calculation (Ref. 23).

5. Electron Transport in Three-Dimensions

Throughout all of the previous one- and two-dimensional electron transport research in which we have participated, a primary objective, in addition to achieving high computational accuracy, has been to achieve a high degree of realism in our modelling capability. In pursuit of the first objective, consideration of realistic three-dimensional device geometries was postponed until the present. Also causing delay in this regard was the unavailability, until recently, of a good three-dimensional electron Monte Carlo program, and finally, the lack of adequate descriptions of realistic microelectronic device geometries. The availability of the ITS[2] Monte Carlo code series has satisfied the first requirement, while the appearance of two papers[25,26] in the 1987 *IEEE Transactions on Nuclear Science*, in which two microelectronic device geometries were published, satisfied the second. The work to be discussed here, resulted in the presentation of a paper at the American Nuclear Society Mathematics and Computation Topical Meeting[24]. This paper will appear in *Nuclear Science and Engineering* in early 1990.

In Ref. 24 is reported the extension of Filippone's S_n method for solving the Spencer-Lewis equation for electron transport to treat three-dimensional multiregion problems. One of the key points of this work was the utilization of the flux continuity condition, which is generalized for multiregion problems by expressing the flux as a function of electron energy rather than pathlength. Such a representation results in a set of S_n/diamond difference equations which are nearly identical in form to conventional S_n/diamond difference equations. The S_n method was then used to calculate electron energy deposition due to 200 keV electron beams incident on problem geometries typical of silicon and gallium-arsenide semiconductor microelectronic devices. Our roles in this work were: 1) to research and define the realistic device geometries; 2) to provide quantitative descriptions of these silicon and gallium-arsenide device geometries for modelling purposes; 3) to define the inputs required by the ACCEPT Monte Carlo calculation; and 4) to aid in the interpretation and presentation of the results.

A fairly extensive discussion of the theory of the three-dimensional S_n calculation method was included by Filippone in Ref. 24, and thus need not be reviewed here. The result of the electron transport calculations were presented in the form of energy deposition resulting from the incidence of electron beam sources on problem geometries typical of semiconductor microelectronic devices. The configurations we chose to work with are based on fairly detailed descriptions of: 1) a silicon (Si) hybrid diode-resistor[25]; and 2) a gallium-arsenide(GaAs) field-effect transistor[26]. The final configurations for the device geometries that were used in our

41

calculations are simplified versions of these, however their essential geometrical character and material compositions were preserved. The Si device geometry is shown in Figure 26.

The S_n code was run for 200 keV electron beam sources incident at a slightly off-center point: $x=0\mu m$, $y=28\mu m$, $z=0\mu m$ for the Si device (as shown in Fig. 25). The incident beam orientation is given by $\theta=90°$, $\phi=45°$, where θ is the polar obliquity with respect to the z-axis and ϕ is the azimuthal angle in the x-y plane. The scattering cross sections were taken to be screened-Rutherford.

We made independent calculations of energy deposition using the ACCEPT module of the Integrated TIGER series(ITS)[2] of coupled electron-photon Monte Carlo codes. The ACCEPT code was run using the screened-Rutherford cross section with the CSDA (no-straggling) option. In this way it was possible to ensure that both the S_N and Monte Carlo calculations were based on the same physical model. Sufficient numbers of Monte Carlo case histories (10^6) were run so that valid benchmark results could be obtained. The estimated standard error was ≤ 1 percent in all of the Monte Carlo tally cells for which the energy deposition exceeded 1 percent of the maximum value. The worst cases, 5-6 percent error estimates, were encountered in only 2 of 129 cells for the Si calculation and 1 of 120 cells for the GaAs calculation. In these instances the energy deposition values were less than 0.1 percent of the peak value.

The energy deposition results, S_n and Monte Carlo, for the Si device mock-up are shown in Figures 27a and 27b, respectively. The data shown result from integration, over the z-coordinate, of the energy deposited per unit volume in the region bounded by the gold cap, and are therefore given in units of MeV/cm^2. The energy deposition results obtained with S_n were found to compare well with results of ACCEPT Monte Carlo calculations. The agreement between the S_n and Monte Carlo results for the GaAs device configuration is qualitatively similar. This comparison is shown in Ref. 24. Computer run times required for the S_n calculations were found to be lower than that required for Monte Carlo by factors ranging from 30 to 50.
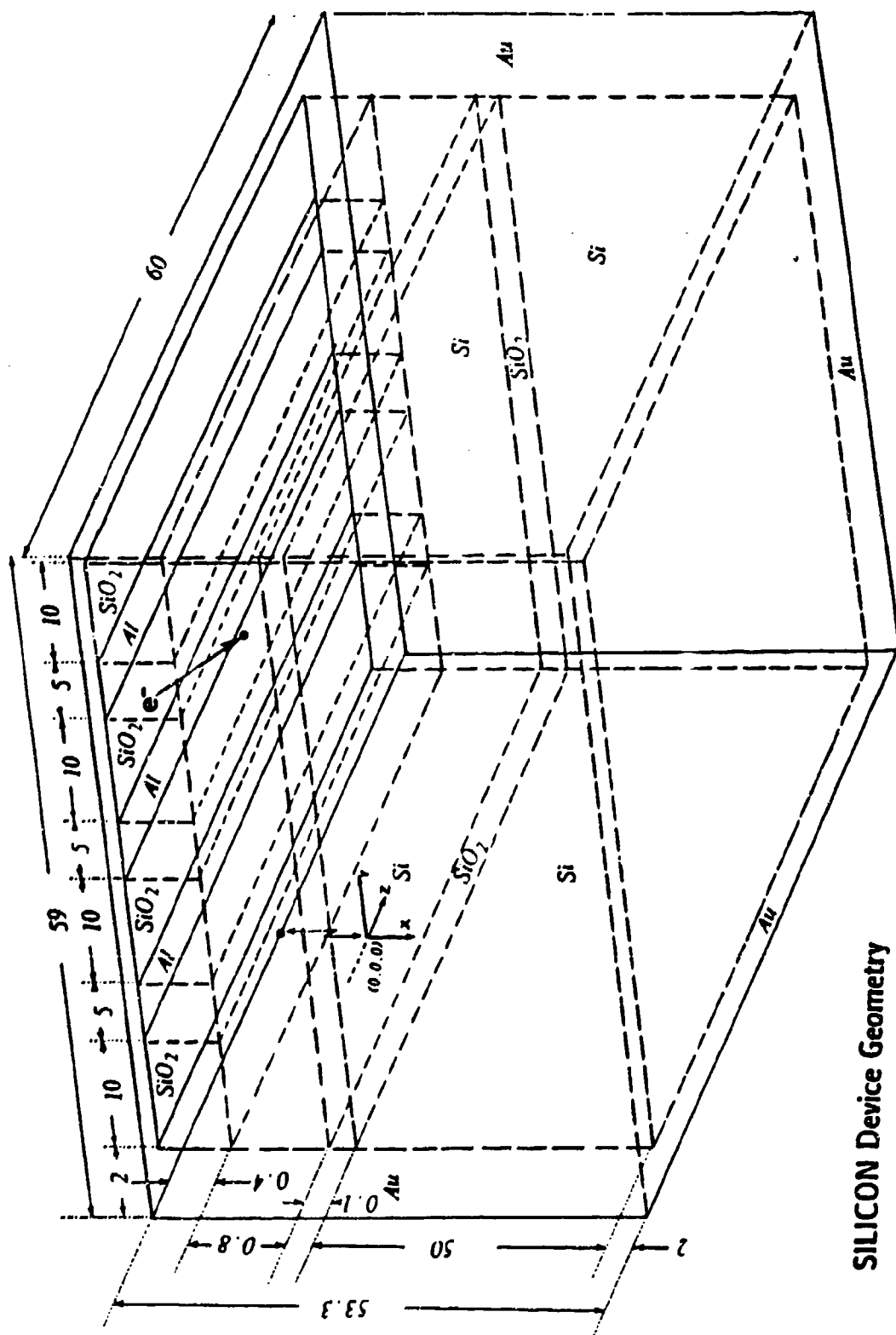
SILICON Device Geometry

Figure 26. Silicon device geometry (not drawn to scale). Length units are μm (Ref. 24).
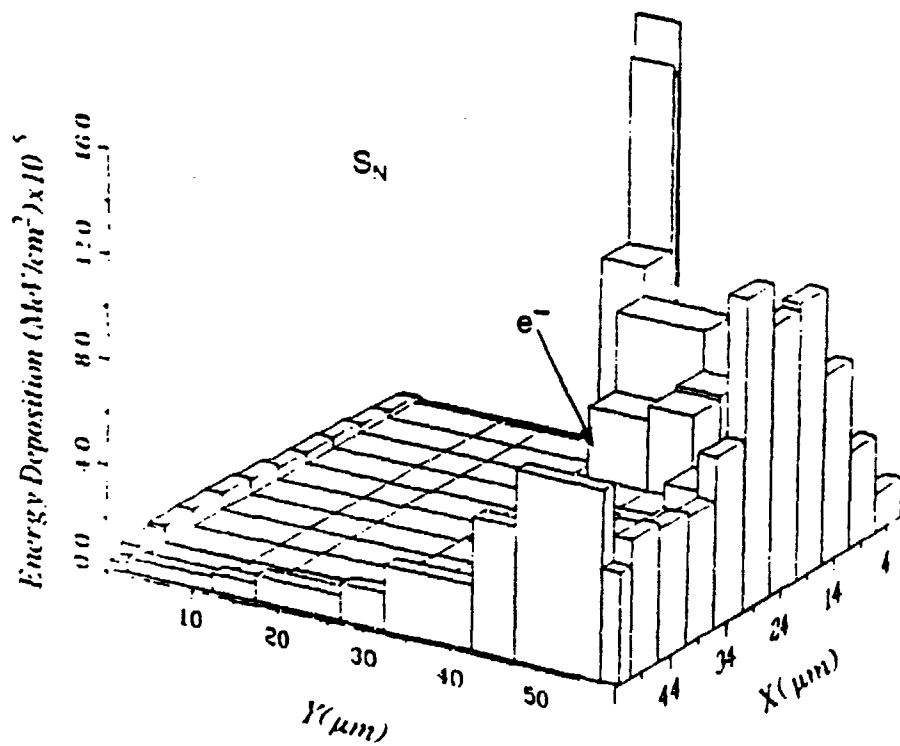
43

Figure 27a.Three-dimensional S_n calculation of energy deposition (MeV/cm^2) resulting from a 45° electron beam incident in a Si device. Source energy = 0.2 MeV (Ref. 24).
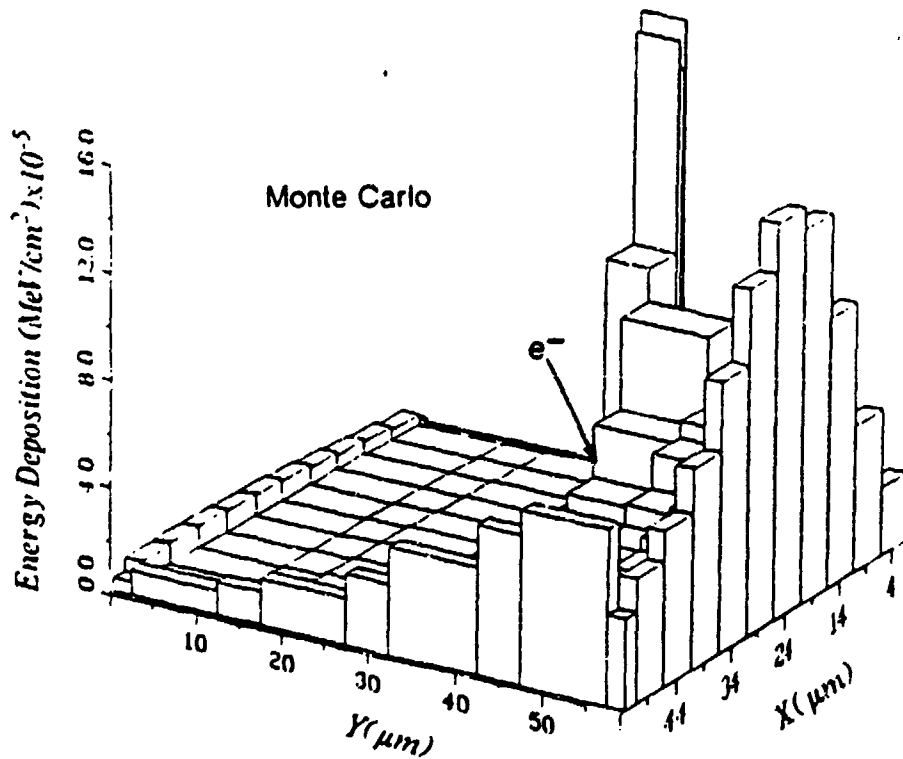

Figure 27b.ITS-ACCEPT[2] Monte Carlo calculation of energy deposition (MeV/cm^2) resulting from a 45° electron beam incident in a Si device. Source energy = 0.2 MeV (Ref. 24).

IV. LOW ENERGY ELECTRON TRANSPORT (0 - 20 eV)

1. Introduction

We have written computer programs and performed calculations to model the inelastic scatter and transport of electrons with very low energy (0 - 20 eV) in SiO_2. The inelastic scatter can occur via two processes: 1) ionization and/or excitation collisions with other electrons; and 2) electron-phonon interactions. The first of these can occur in SiO_2 only for electron energies above the ionization threshold of 8.9 eV. It is believed that the second of these processes, interactions with phonons, can occur across the energy range 0 - 20 eV. Our principal activities in this research area have consisted of three projects. The first of these is the interpretation of electron-phonon scattering theory and its translation into a set of numerical algorithms, and a computer program (PHONON), for the evaluation of basic scattering parameters, such as scattering cross section, scattering angle distributions, and effective stopping powers. The second task in this project is the incorporation of the above calculated parameters in a Monte Carlo transport code (LOWEND) for electrons in the 0 - 20 eV energy range in SiO_2. The third of these is the application of the method of discrete ordinates (S_n), a determininstic method for the numerical solution of the transport equation, to electron-phonon scattering.

2. PHONON: Computer Program for the Evaluation of the Basic Parameters of Electron-Phonon Scattering

Electrons of very low energy, below ionization threshold, can undergo inelastic scatter through the electron-phonon interaction. These are interactions with the lattice and result in phonon emission or absorption. Specific information relating to the evaluation of electron-phonon cross sections, stopping powers and scattering angles comes to us by way of the both private communication and open literature[27]. The theoretical basis of the contents of this section is adapted from the work of Ashley[27] and applies to electron-phonon scattering in SiO_2. With this theoretical basis, we designed the numerical algorithms and wrote the computer program PHONON for the evaluation of the cross sections, stopping powers and scattering angle. Some of the results of our calculations to be shown here also appear in Ref. 28. Electron-phonon interactions occur in two modes, longitudinal (LO) and acoustic (AC). There is a total of 6 interaction modes, 4 LO and 2 AC. This arises from the fact that both the LO and AC modes may result in phonon emission (electron energy gain) or phonon

45

absorption (electron energy loss), and there are 2 discrete phonon energies to consider for SiO_2 ($\hbar\omega_p = 0.068$ eV and 0.153 eV[ω_p is the phonon frequency]).

2.1 LO Modes

2.1.1 Inverse Mean Free Path

The inverse mean free paths for the LO modes are given by the following expression[27]:

$$\lambda^{-1}_{\pm,LO}(E) = \frac{e^2\omega_p}{\hbar v^2}[\frac{1}{\epsilon_\infty} - \frac{1}{\epsilon_0}]\left(n_\omega + \frac{1}{2} \pm \frac{1}{2}\right)\int_{W_1^\pm(E)}^{W_2^\pm(E)} \frac{dq}{q}$$

$$= \frac{e^2\omega_p}{\hbar v^2}[\frac{1}{\epsilon_\infty} - \frac{1}{\epsilon_0}]\left(n_\omega + \frac{1}{2} \pm \frac{1}{2}\right)\ln\frac{W_2^\pm(E)}{W_1^\pm(E)} \ , \tag{26}$$

where

$\lambda^{-1}_{+,LO}$ = inverse mean free path for phonon emission,

$\lambda^{-1}_{-,LO}$ = inverse mean free path for phonon absorption,

ω_p = phonon frequency,

v = incident electron velocity,

ϵ_∞ = SiO_2 dielectric constant in the optical region,

ϵ_0 = SiO_2 static dielectric constant,

n_ω = $\left(\exp(\hbar\omega/k_BT) - 1\right)^{-1}$,

k_BT = .025 eV,

q = wave number corresponding to electron energy gain (+) or loss (-) .

The total inverse mean free path (cross section) for the LO mode is then given by

$$\lambda^{-1}_{LO} = \lambda^{-1}_{+,LO} + \lambda^{-1}_{-,LO} \ . \tag{27}$$

The upper and lower limits of the integral in Eq. 26 correspond, respectively, to the maximum and minimum possible q values: if the incident electron kinetic energy is denoted as E, then

$$W_2^\pm(E) = \min\left\{k_0\left(1 + \sqrt{1 \mp \frac{\hbar\omega_p}{E}}\right), k_{BZ}\right\} , \tag{28a}$$

and

46

$$W_1^\pm(E) = \pm k_0\left(1 - \sqrt{1 \mp \frac{\hbar\omega_p}{E}}\right), \tag{28b}$$

where

$$\hbar k_0 \quad = \sqrt{2m^*E} \,,$$

$$m^* \quad = \text{electron effective mass,}$$

and $\quad k_{BZ}$ is the wavenumber corresponding to the Brillouin zone threshold energy.

The quantity $[\frac{1}{\epsilon_\infty} - \frac{1}{\epsilon_0}]$ has two values, 0.0816 for $\hbar\omega_p = 0.068$ eV and 0.112 for $\hbar\omega_p = 0.153$ eV.

2.1.2 Scattering Angle Distribution

The distribution of scattering angle cosines, $\cos\theta_\pm$, is determined from momentum and energy conservation and is given by[27]

$$\cos\theta_{\pm,LO}(E) = \frac{1 - q^2/2k_0^2 \pm \hbar\omega_p/2E}{\sqrt{1 \mp \hbar\omega_p/E}} \,. \tag{29}$$

where, as before, the momentum tranfer wave number, q, ranges from $W_1^\pm(E)$ to $W_2^\pm(E)$.

The average scattering angle cosine $< \cos\theta_{\pm,LO}(E)>$ is obtained from

$$< \cos\theta_{\pm,LO}(E)> \;=\; \int_{W_1^\pm(E)}^{W_2^\pm(E)} \frac{dq}{q}(1 - q^2/2k_0^2 \pm \hbar\omega_p/2E) \Big/ \sqrt{1 \mp \hbar\omega_p/E} \int_{W_1^\pm(E)}^{W_2^\pm(E)} \frac{dq}{q}$$

$$= \frac{(1 \mp \hbar\omega_p/2E)\ln[W_2^\pm(E)/W_1^\pm(E)] - \frac{1}{4k^2}[W_2^\pm(E)^2 - W_1^\pm(E)^2]}{(\sqrt{1 \mp \hbar\omega_p/E})\,\ln[W_2^\pm(E)/W_1^\pm(E)]} \,. \tag{30}$$

2.1.3 Stopping Power

The expression for the LO mode stopping power is given by[27]

$$\frac{dE}{dx}\Big|_{LO_\pm} = \frac{e^2\omega_p}{v^2}[\frac{1}{\epsilon_\infty} - \frac{1}{\epsilon_0}]\left(n_\omega + \frac{1}{2} \pm \frac{1}{2}\right)\ln\frac{W_2^\pm(E)}{W_1^\pm(E)} \,. \tag{31}$$

2.2 AC Modes

2.2.1 Inverse Mean Free Path

The inverse mean free paths for the AC modes are given by[27]

$$\lambda^{-1}_{\pm\,AC} = \frac{3m^*}{4\pi MN_c\hbar^2 k_0} \int_0^{q^{\pm}_{max}} dq\,\frac{q^3}{\omega_p(q)}\,[n(q) + \tfrac{1}{2}\pm\tfrac{1}{2}] \qquad (32)$$

where M and N_c are, respectively, the mass and density of the SiO$_2$ unit cell and

$$q^{\pm}_{max} = \begin{cases} 2k_0 \mp 2m^*C_s/\hbar & ,\ q < k_{BZ} \\ k_0\left(1 + \sqrt{1\mp\hbar C_s k_{BZ}/E}\right) & ,\ q \geq k_{BZ} \end{cases} \qquad (33)$$

$$n(q) = \begin{cases} \left(e^{\alpha q}-1\right)^{-1} & ,\ q < k_{BZ} \\ \left(e^{\alpha k_{BZ}}-1\right)^{-1} & ,\ q \geq k_{BZ} \end{cases} \qquad (34)$$

$$\omega_p(q) = \begin{cases} C_s q & ,\ q < k_{BZ} \\ C_s k_{BZ} & ,\ q \geq k_{BZ} \end{cases} \qquad (35)$$

C_s = velocity of sound in SiO$_2$, and

$$\alpha \equiv \hbar C_s/k_B T \quad .$$

2.2.2 Scattering Angle Distribution

For the AC modes the distribution of scattering angle cosines $\cos\theta_{\pm}$ is also determined from momentum and energy conservation and is given by[27]

$$\cos\theta_{\pm,AC}(E) = \frac{1-q^2/2k_0^2 \pm \hbar\omega_p(q)/2E}{\sqrt{1\mp\hbar\omega_p(q)/E}} \quad . \qquad (36)$$

where the phonon frequency $\omega_p(q)$ is now dependent on the the momentum transfer wave number, q, as given in Eq. 35. In contrast to the LO case, an exact analytical expression cannot be derived for the average scattering angle cosine $< \cos\theta_{\pm,AC}(E)>$.

$$\langle \cos\theta_{\pm,AC}(E)\rangle = \int_0^{q_{max}^{\pm}} dq \frac{\frac{q^3}{\omega_p}[n(q)+\frac{1}{2}\pm\frac{1}{2}](1-q^2/2k_0^2\pm\hbar\omega_q/2E)}{\sqrt{1\mp\hbar\omega_p/E}} \Big/ \int_0^{q_{max}^{\pm}} dq \frac{q^3}{\omega_p}[n(q)+\frac{1}{2}\pm\frac{1}{2}] \quad (37)$$

must be evaluated numerically.

2.2.3 Stopping Power

The expression for the AC mode stopping power is given by[27]

$$\frac{dE}{dx}\Big|_{AC_\pm} = \frac{3m^*}{4\pi MN_c\hbar k_0} \int_0^{q_{max}^{\pm}} dq\, q^3\, [n(q) + \tfrac{1}{2}\pm\tfrac{1}{2}] . \quad (38)$$

2.3 Numerical Evaluation of Scattering Parameters

The above expressions for the electron-phonon inverse means free paths, scattering angle distributions and stopping powers were evaluated in our computer program, PHONON. Since the expressions for the longitudinal mode parameters (given by Eqs 26,30,31) are analytic and do not involve complicated numerical evaluation of special functions, tables of these quantities as functions of electron energy were generated in a straightforward manner. Algorithm development for numerical evaluation of the acoustic mode parameters was somewhat more involved. The integral expressions (Eqs. 32,37,38) could not be evaluated analytically without approximation. We divided the region of integration into 3 sub-regions: 1) 0 to q_l, where the energy fraction $\hbar\omega_q/k_BT = 0.005$; 2) q_l to k_{BZ} ; and 3) k_{BZ} to q_{max} .

In the first sub-region, recalling Eq. 35, we made the following approximations :

$$\left(1 \mp \hbar C_s q/E\right)^{-1/2} \approx 1 \pm \hbar C_s q/2E , \quad (39)$$

and

$$n(q) \approx \frac{k_BT}{\hbar C_s q} . \quad (40)$$

With these approximations, the integrands of Eqs. 32,37,38 become simple algebraic functions of q which are then evaluated exactly.

The second integration sub-region, q_l to k_{BZ}, is handled with our adaptive Gaussian

49

quadrature numerical integration program, AQG4. This program employs the method of interval splitting to perform the numerical integration to within a user specified accuracy. If such accuracy is unattainable, due to the functional form of the integrand or computer limitation. AQG4 informs the calling program through informative diagnostics.

Finally, in the third sub-region, both $\omega_p(q)$ and $n(q)$ take on constant values, so that the integrals of Eqs. 32,37,38 are evaluated analytically. We made extensive calculations, for the 4 LO and 2 AC interaction modes, based on the above theory for the electron-phonon scattering cross section, mean scattering angle cosine and stopping power in SiO_2 for subionization electrons ($E < 8.9$ eV). In Fig. 28 we show a plot of the total scattering cross section, averaged over the LO and AC modes. Fig. 29 is a plot of the mean scattering angle cosine averaged over the LO and AC phonon emission modes (solid curve). The dashed curves show the contributions on the LO and AC emission components individually. Finally, Fig. 30 is a plot of the electron-phonon interaction stopping power, averaged over the 6 modes.

Tabulations of the electron-phonon cross section, average scattering angle cosine and stopping power were compiled using the PHONON program and then incorporated into our low energy electron transport Monte Carlo trajectory simulation program, LOWEND (to be discussed in the next section). It was then possible to obtain, through trajectory simulation, electron energy spectra, energy loss(gain), and drift velocity values in the presence of an applied electric field for subionization electrons in SiO_2.

Figure 28. Total electron scattering cross section, averaged over the longitudinal optical and acoustical phonon excitation modes, in SiO_2 for the sub-ionization threshold energy region (Ref. 28).

Figure 29. Mean scattering angle cosine for electrons with energy < 8.89 eV in SiO_2 for longitudinal optical phonon (LOE) and acoustical phonon (ACE) emission. The solid curve is the weighted mean cosine over the two phonon excitation modes (Ref. 28).
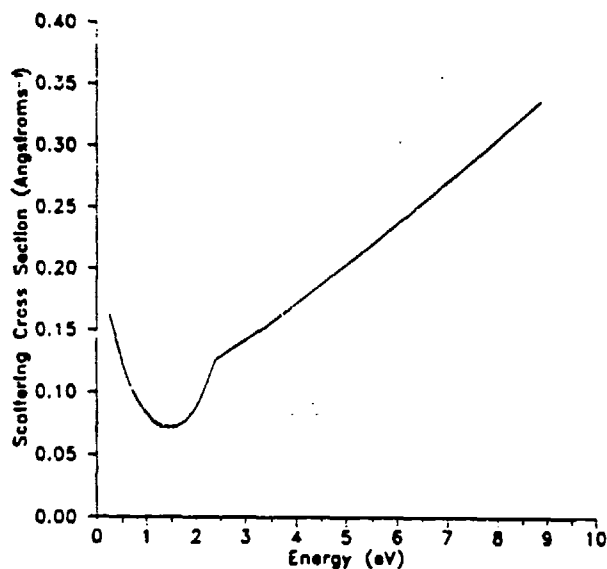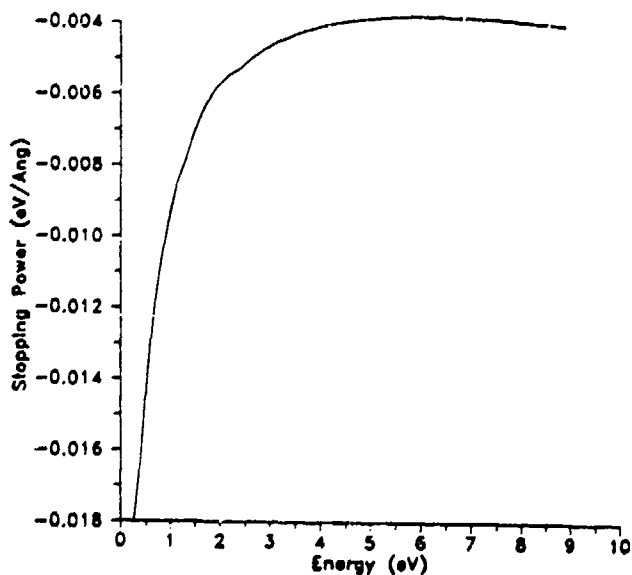

Figure 30. Electron stopping power averaged over the longitudinal optical and acoustical phonon excitation modes, in SiO_2 for the sub-ionization threshold energy region (Ref. 28).
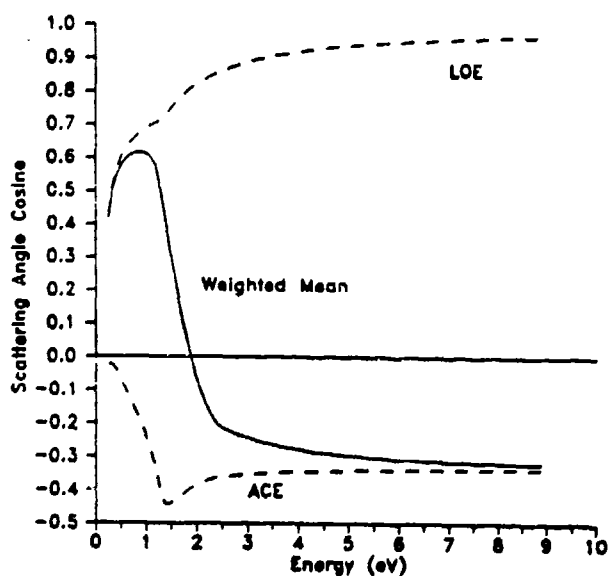
3. LOWEND: Monte Carlo Simulation Program for Subionization (≤8.9 eV) Electron Transport

3.1 Overview

The physical parameters governing the transport process for low energy (subionization) electrons were calculated with program PHONON and then supplied through a set of tables to our single scatter Monte Carlo program LOWEND[28]. These tables consisted of the following energy-dependent entries for the electron-phonon interaction: 1) total inverse mean free path, λ^{-1}; 2) total stopping power, dE/dx; 3)scattering angle average cosine, $<\cos \omega>$. The total inverse mean free path and stopping power values were obtained by summation over the 4 longitudinal and 2 acoustic phonon emission and absorption modes, while the scattering angle cosine values were obtained with a summation over the 6 modes weighted by their respective probabilities of occurrence.

The main features of the LOWEND code are that it accounts for: 1) electron energy loss and scatter with both LO and AC phonons; and 2) energy loss/gain in the presence of an applied electric field. With this code it is possible to obtain, through trajectory simulation, electron energy spectra, energy loss(gain) or ΔE distributions, and drift velocity values in the presence of an applied electric field for subionization electrons which appear in SiO_2 as a result of inelastic scattering processes. The electric field values for which this program has been tested range from 0 to 10 MV/cm. In this calculation electron trajectories are simulated in direct analog Monte Carlo fashion. It was found that 5000 - 10000 electron case histories were sufficient to produce statistically adequate results for energy spectra, while 1000 histories proved sufficient for determination of averaged quantities such as drift velocity. The above estimates appied provided that the case histories were allowed to run for a sufficiently large number of simulated collisions to produce quasi-equilibrium conditions (small variation of energy spectrum shape and magnitude) over a large spatial region (300-1000 Å). This condition gave rise to a "rule of thumb" that 600-1000 collisions per case history were adequate for electric field (ε) values below 5 MV/cm, while a larger number, ~3000 for determination of averaged quantities and ~10000 for energy spectra, were required for ε = 10 MV/cm. Typical run times for the Monte Carlo program are on the order of 0.6 hr/(1000 histories) on the AFGL VAX 8650 computer.

3.2 Electron Trajectories in the Presence of an Applied Electric Field

The action of the applied field, $\mathscr{E}$, is to transform the electron trajectory path segments into parabolic sections. For short path segments, this curvature can be ignored and the calculations can be made on the basis of a straight line segment approximation. The length of the segment, Δs, is chosen by random selection from the path length probability distribution (via the usual inversion of the exponential attenuation rule, $\lambda(E)$ is taken to be the mean free path). The energy change is then given by

$$\Delta E = \int_c \underline{F} \cdot \underline{ds} \doteq \int^{\Delta s/v_0} \underline{F} \cdot \underline{v} dt$$

$$= \int^{\Delta s/v_0} \underline{F} \cdot (\underline{v}_0 \hat{v} + \underline{a}t) dt \quad . \tag{41}$$

where
$$\underline{F} = \frac{dE}{dx} \hat{v} + e\mathscr{E}\hat{z}, \qquad \frac{dE}{dx} = \text{electron stopping power,}$$

$$\underline{a} = \frac{1}{m}\frac{dE}{dx} \hat{v} + \frac{e\mathscr{E}}{m}\hat{z}, \qquad e = \text{electron charge,}$$

$$\hat{v} \cdot \hat{z} = \cos\theta = \text{velocity direction cosine along } \mathscr{E} \text{ direction.}$$

Insertion and integration yields

$$\Delta E = \left(\frac{dE}{dx} + e\mathscr{E}\cos\theta\right)\Delta s + \left(|\frac{dE}{dx}|^2 + (e\mathscr{E})^2 + 2\frac{dE}{dx}e\mathscr{E}\right)\frac{\Delta s}{2mv_0^2} \quad . \tag{42}$$

From these expressions one can calculate the velocity components and position coordinates.

For longer Δs segments, which admit of curvature and larger energy change, we have used a five sub-segment approximation to the path integral for energy change. In this procedure the values of E, $\cos\theta$, $\lambda(E)$, dE/dx and the position and velocity coordinates are updated in each step. The resulting energy change is given by

$$E_f - E_i = \sum_k \Delta E_i = \sum_k v_0(\tau_k - \tau_{k-1})\left(\frac{dE}{dx} + e\mathscr{E}\cos\theta_k\right) +$$

$$\left(|\frac{dE_k}{dx}|^2 + (e\mathscr{E})^2 + 2\frac{dE_k}{dx}e\mathscr{E}\cos\theta_k\right)\left(\frac{\tau_k^2}{2m_k} - \frac{\tau_{k-1}^2}{2m_{k-1}}\right) \quad . \tag{43}$$

where $\qquad r_k = r_{k-1} + \dfrac{\Delta s_k}{5\sqrt{2E_k/m_k}}$ and $r_0 = 0$.

The velocity component (v_{zk}) in the direction of the electric field ($\mathcal{E}$) is given by

$$v_{zk} = \left(v_0 + \frac{1}{m^*}\frac{dE}{dx}\frac{\Delta s}{5v}\right)_{k-1}\cos\theta_{k-1} + \left(\frac{e\mathcal{E}}{m^*}\frac{\Delta s}{5v}\right)_{k-1} \quad . \tag{44}$$

3.3 LOWEND Calculations of Electron Energy Spectra

One of the results obtainable with a LOWEND calculation is the determination of kinetic energy equilibrium spectra in the presence of an applied electric field. When we considered electron transport exclusively in the subionization energy region, it was found that for a 5 eV injection energy into SiO_2, energy equilibrium was well established at a depth of 500 $\overset{\circ}{A}$ for a wide range of electric field values. Fig. 31 shows calculated electron kinetic energy spectra for 3 values of $\mathcal{E}$, (0.5, 4 and 10)x10^6V/cm. When we extended the electron-phonon cross section, scattering angle and stopping power tables to the 8.9 - 20 eV range, ionizing collisions occurred. The ionization cross sections[28] used in this calculation, supplied by ORNL, are shown in Fig. 32. Fig. 33 shows the electron energy spectrum in the presence of a 10^7V/cm electric field. This result was obtained using electron-phonon parameter tables extended to 20 eV and the ORNL inelastic cross sections. As can be seen, the high energy portion of the spectrum(>8.9 eV) accounts for a significant fraction. It was found that for fields in excess of $\sim$7x10^6V/cm., our predictions of the amount of electron multiplication exceeded experimental observation. An effort is presently underway to reconcile these differences.
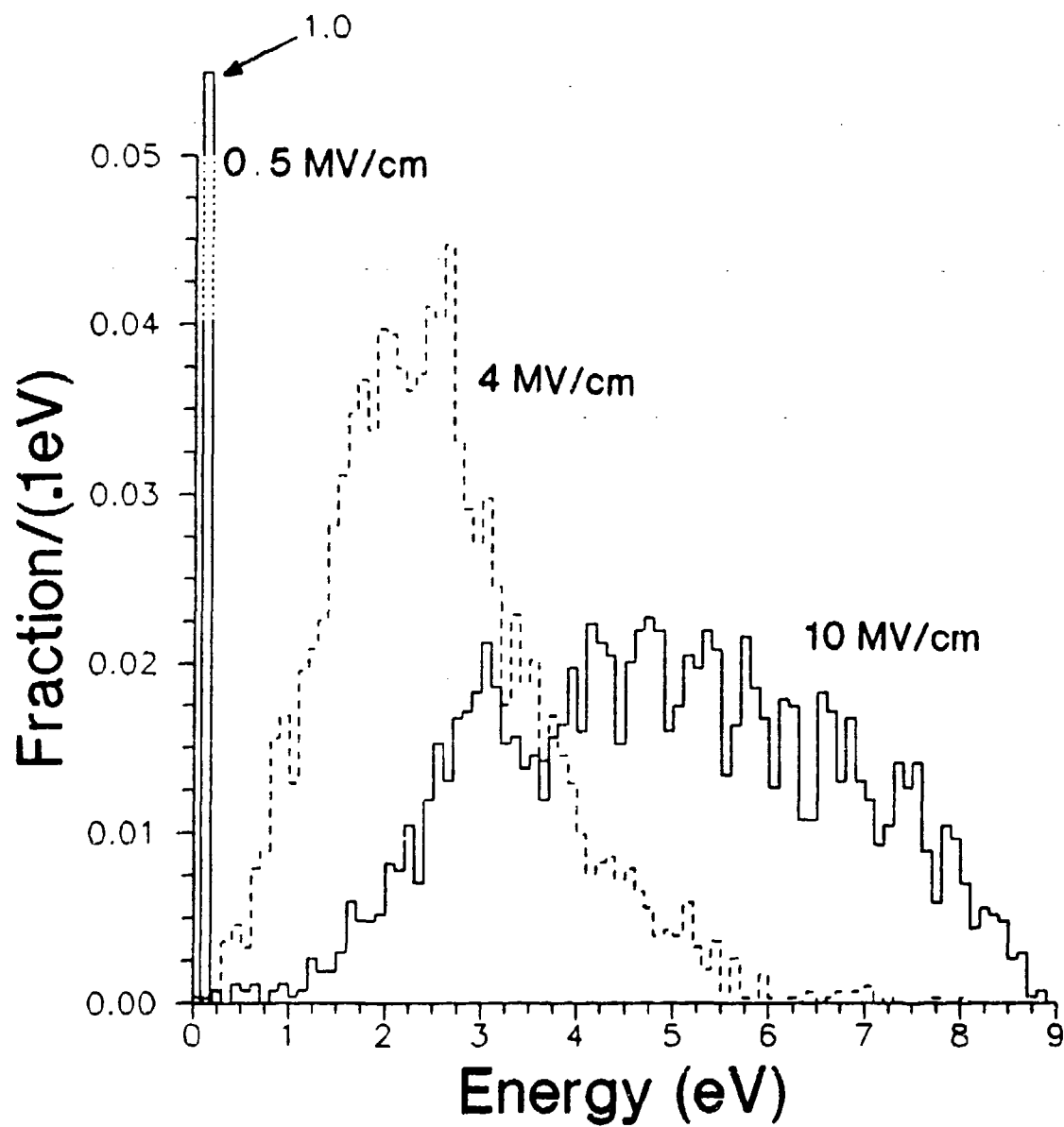
Figure 31. Kinetic energy equilibrium spectra in SiO_2. as calculated by LOWEND. for 3 values of the applied electric field.
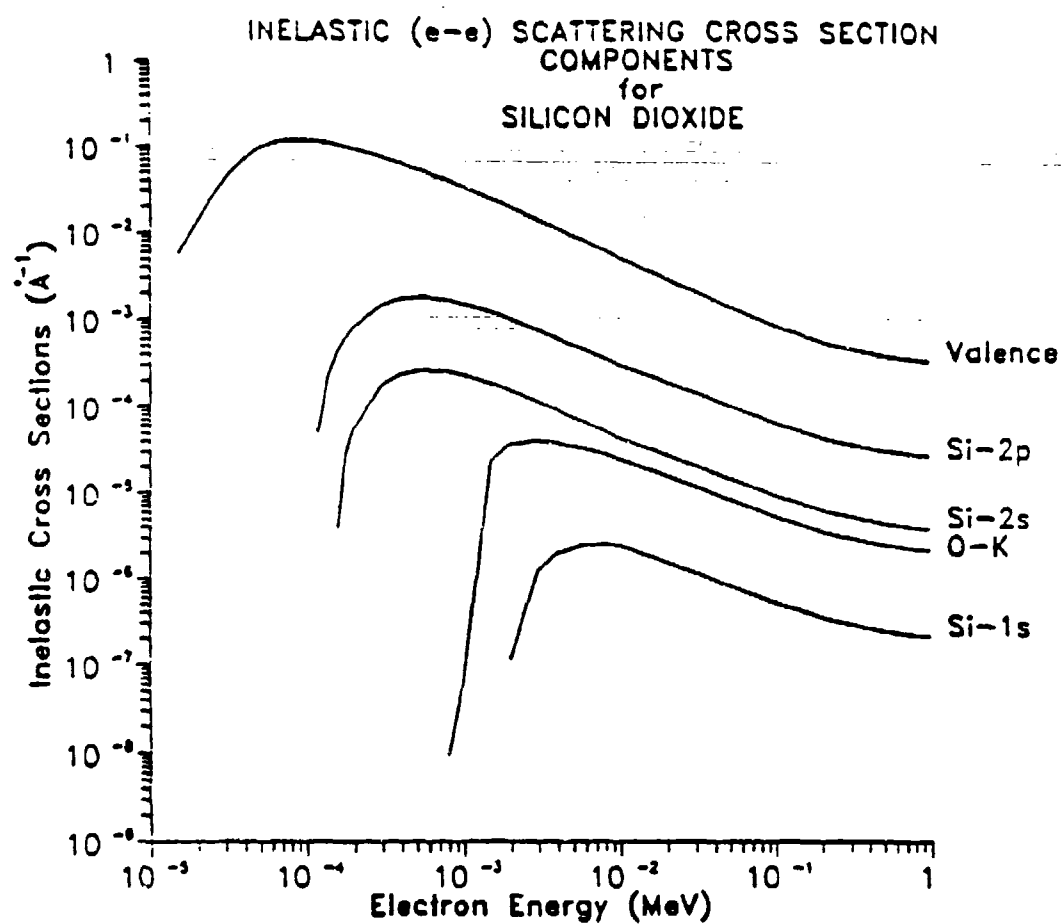
Figure 32. Inelastic electron-electron scattering cross section components for SiO_2 (Ref. 28).
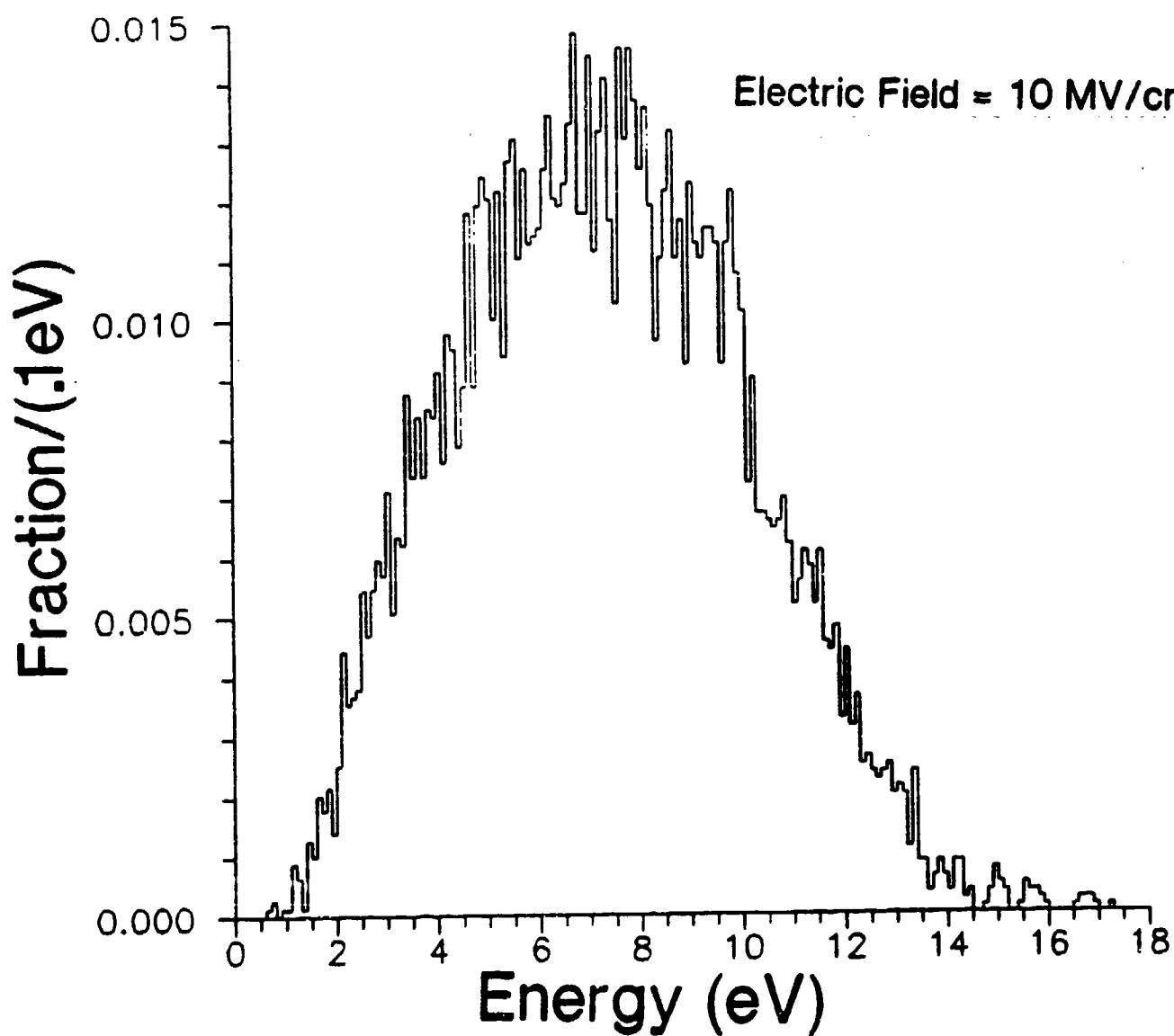
Figure 33. Kinetic energy spectrum, as calculated by LOWEND, for applied field of 10^7V/cm at 500 Å depth in SiO_2. High energy tail above 8.9 eV exists due to small cross section for secondary ionization at these energies.

4. Transport Equation Solution for Electron-Phonon Scattering by the Method of Discrete Ordinates (S_n)

Discrete ordinates electron transport calculations were made using the standard S_n code, ONETRAN[1], for low energy (subionization) electrons in SiO_2. Preparation for these calculations involved reformulating the electron-phonon transport parameters, cross-section and stopping power into the multigroup format compatible with the S_n method. As was done for the Monte Carlo calculations reported in the previous section, these multigroup parameters were derived separately for the longitudinal(LO) and acoustic(AC) mode.

4.1 LO Modes

4.1.1 Group-to-Group Scattering Cross Sections

Making use of Eqs. 26, 28a,b and 29, we arrived at expressions for the group-to-group energy transfer cross sections.

For energy loss:

let E_g = initial electron energy, and E_g' = final electron energy , so that $E_g > E_g'$.

Then the downscatter cross section is

$$\sigma_-^{LO}(E_g \to E_g') = \begin{cases} A\omega\, n_\omega\, \ln[q_{gg'}/W_1^-(E_g)] & ; \quad W_1^-(E_g) \leq q_{gg'} \leq W_2^-(E_g) \\ 0 & ; \text{ elsewhere} \end{cases} \tag{45}$$

where

$$\hbar q_{gg'} = \sqrt{2m^*(E_g\text{-}E_g')} \quad .$$

There are two cross sections $\sigma_-^{LO}(E_g \to E_g')$ corresponding to the two values of $\hbar\omega$.

Similarly, for $E_g < E_g'$ (energy upscatter) we have

$$\sigma_+^{LO}(E_g \to E_g') = \begin{cases} A\omega\, (n_\omega+1)\, \ln[q_{gg'}/W_1^-(E_g)] & ; \quad W_1^+(E_g) \leq q_{gg'} \leq W_2^+(E_g) \\ 0 & ; \text{ elsewhere} \end{cases} \tag{46}$$

where $\hbar q_{gg'} = \sqrt{2m^*(E_g'\text{-}E_g)}$.

As in the phonon absorption case, there are two cross sections $\sigma_+^{LO}(E_g \to E_g')$ corresponding to the two values of $\hbar\omega$.

58

4.1.2 Group-to-Group Scattering Angle

The scattering angle cosines corresponding to the above are given by

$$\mu_{gg'}\pm = \frac{1-q^2_{gg'}/2k^2_g \pm \hbar\omega/2E_g}{\sqrt{1\mp\hbar\omega/E_g}} \qquad (47)$$

where

$$\hbar k_g = \sqrt{2m^*E_g} \quad .$$

Expressions were derived for the Legendre expansion coefficients of the angular scattering cross section for electron-phonon interactions. This was necessitated by the fact that most discrete ordinates algorithms and codes accept and utilize the angular scattering data in this format. The analysis for the longitudinal optical (LO) mode downscatter in energy from group g to group g' ($E_g > E_g'$) is shown below (the derivation for upscatter was similarly derived).

The average scattering angle cosine is given in terms of integrals over the momentum transfer, q, by:

$$<\mu^-_{gg'}> = \frac{\int_{w^-_{1,gg'}}^{w^-_{2,gg'}} \frac{dq}{q} (1-q^2/2k^2_g + \hbar\omega/2E_g)}{\sqrt{1-\hbar\omega/E_g} \int_{w^-_{1,gg'}}^{w^-_{2,gg'}} \frac{dq}{q}} \quad , \qquad (48)$$

where

$$w^-_{1,gg'} = \frac{1}{\hbar}\sqrt{2m^*(E_g-E_g'+1/2)} \quad , \qquad (49a)$$

$$w^-_{2,gg'} = \frac{1}{\hbar}\sqrt{2m^*(E_g-E_g'-1/2)} \quad , \qquad (49b)$$

with the restrictions that

$$\min[w^-_{1,gg'}] = W^-_1(E_g) = k_g\left(1-\sqrt{1+\frac{\hbar\omega}{E_g}}\right) , \qquad (50a)$$

and

$$\max[w^-_{2,gg'}] = W^-_2(E_g) = \min\left\{k_g\left(1+\sqrt{1+\frac{\hbar\omega}{E_g}}\right), k_{BZ}\right\} , \qquad (50b)$$

where $\hbar k = \sqrt{2m^*E}$, m^* is the electron effective mass and k_{BZ} is the wavenumber corresponding to the Brillouin zone threshold energy.

59

The Legendre expansion for the angular scattering cross section is

$$\sigma(\mu) = \sum_{l=0}^{N} (l+1/2)\sigma_l P_l(\mu) \ , \qquad (51)$$

where

$$\sigma_l = \int_{-1}^{+1} \sigma(\mu) \, P_l(\mu) \ d\mu \ . \qquad (52)$$

With the following definition for the n-th moment of μ ,

$$<\mu^n> \equiv \frac{\displaystyle\int_{-1}^{+1} \sigma(\mu) \, \mu^n \ d\mu}{\displaystyle\int_{-1}^{+1} \sigma(\mu) \ d\mu} \ , \qquad (53)$$

the first five Legendre expansion coefficients are given as

$$\sigma_0 = \int_{-1}^{+1} \sigma(\mu) \ d\mu \ . \qquad (54a)$$

$$\sigma_1 = <\mu>\sigma_0 \ , \qquad (54b)$$

$$\sigma_2 = \tfrac{1}{2}(3<\mu^2> - 1)\sigma_0, \qquad (54c)$$

$$\sigma_3 = \tfrac{1}{2}(5<\mu^3> - 3<\mu>)\sigma_0, \qquad (54d)$$

$$\sigma_4 = \tfrac{1}{8}(35<\mu^4> - 30<\mu^2> +3)\sigma_0. \qquad (54e)$$

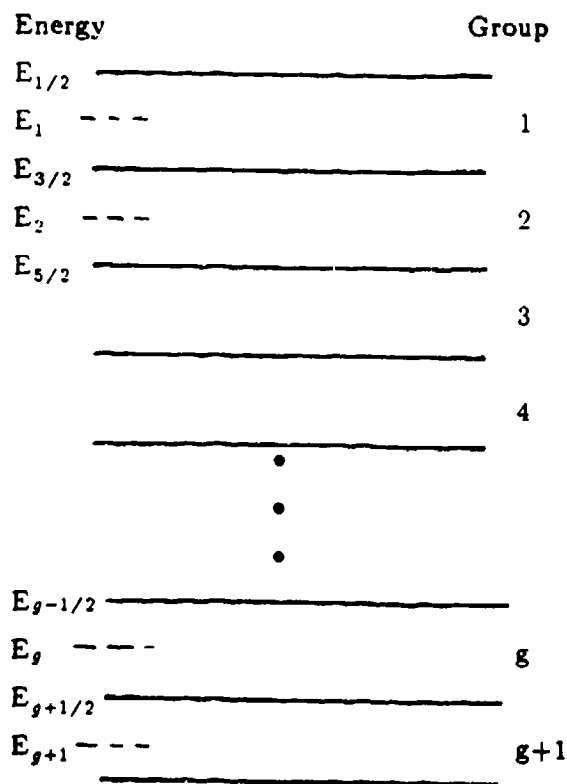| Energy		Group
$E_{1/2}$	————	
E_1	- - -	1
$E_{3/2}$	————	
E_2	- - -	2
$E_{5/2}$	————	
		3
	————	
		4
	————	
	$\bullet$	
	$\bullet$	
	$\bullet$	
$E_{g-1/2}$	————	
E_g	- - -	g
$E_{g+1/2}$	————	
E_{g+1}	- - -	g+1
	————	

Figure 34. Energy group structure

for subionization electrons, SiO_2

60

The above moments of μ were calculated with analytical integrations of the form

$$<(\mu^{-}_{gg'})^n> = \frac{\displaystyle\int_{w^{-}_{1,gg'}}^{w^{-}_{2,gg'}} \frac{dq}{q} (1-q^2/2k^2_g+\hbar\omega/2E_g)^n}{\sqrt{1-\hbar\omega/E_g} \displaystyle\int_{w^{-}_{1,gg'}}^{w^{-}_{2,gg'}} \frac{dq}{q}} . \qquad (55)$$

Program PHONON (see sec. 2 of this chapter), which was originally written to calculate electron-phonon cross sections for the LOWEND (see sec. 3 of this chapter) Monte Carlo calculations, was modified to incorporate the above algorithms for the Legendre expansion coefficients.

4.2 AC Modes

The acoustic mode (AC) cross sections were treated differently from the LO cross sections. The simplifying assumption of isotropic scattering was made for the angular dependence of the AC cross sections. This arises from the following considerations. The maximum energy transfer in an AC collision is ~ 0.02 eV. The average scattering angle cosine for these individual collisions is ~ 0.3 and is fairly constant until the energy approaches values less than 2 eV. For a reasonably sized energy group width, say 0.1 eV, outscatter to other groups would not occur in any single collision. It is known that many such individual collisions can occur (for much of the energy range of interest $\sigma_{AC}/\sigma_{LO} \sim 10$). Thus it was decided to treat the AC mode case using the continuous slowing-down approximation. Since we already had expressions for the AC mode stopping power (up- and down-scatter) as given by Eq. 38, we could calculate the cross section for transfer between adjacent energy groups as

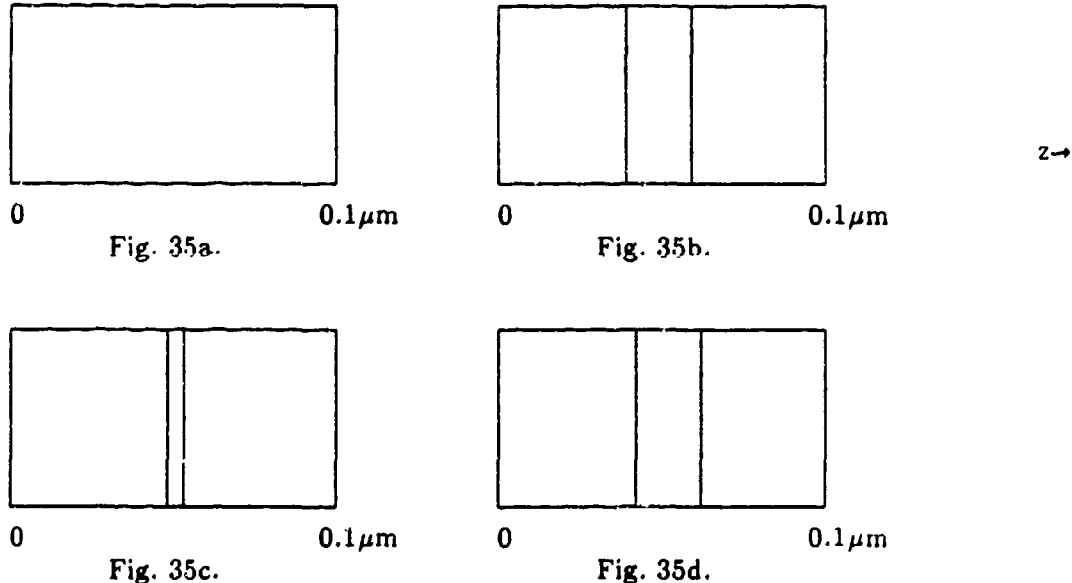$$\sigma^{\pm}_{AC,g} = (\frac{dE}{dx})^{\pm}_g/\Delta E_g , \qquad (56)$$

where $(\frac{dE}{dx})^{\pm}_g$ is the AC mode stopping power.

The above cross section (Eq. 56) may be considered as representing a composite of many

61

individual collisions, the number of which depends on the energy group width ΔE. This composite "collision" consists of many turn-around collisions which average out to a scattering angle cosine ~ 0 (isotropic scatter). This algorithm was also incorporated in program PHONON. In addition, a section of code was written for PHONON to convert the cross section Legendre coefficient table into a format compatible for use with ONETRAN.

4.3 Results of S_n Calculations

A series of preliminary electron transport calculations were made with ONETRAN for electron-phonon scattering. The calculations were done in the absence of an electric field. The electron source energy was taken to be 5 eV. The calculations were made with 100 uniformly spaced energy groups over the energy range 0 to 10 eV. The thick ass of the scattering material, SiO_2, was taken to be 0.1 μm, with 100 spatial discretization intervals of equal width ($\Delta z = 0.001$ μm). Four source geometries were considered: 1) planar(at $z = 0$) monodirectional (along z-direction) source [fig.35a]; 2) monodirectional (along z) source uniformly distributed from $z = 0.04$ μm to $z = 0.06$ μm [fig. 35b]; 3) monodirectional (along z) source of width Δz centered at $z = 0.0505$ μm [fig. 35c]; 4) isotropic (in direction) source uniformly distributed from $z = 0.04$ μm to $z = 0.06$ μm [fig. 35d].

0   0.1μm   0   0.1μm
   Fig. 35a.   Fig. 35b.

z→

0   0.1μm   0   0.1μm
   Fig. 35c.   Fig. 35d.

Sample plots of the electron flux profiles as calculated for 5 energies are shown in Figs. 36 and 37 for the plane perpendicular and isotropic source configurations shown in Figs. 35a and 35d, respectively.

Figure 36. Electron flux vs. depth profiles, as calculated with ONETRAN[1] for electron-phonon scattering, for 5 electron energies, due to the incidence of a 5 eV monodirectional electron source normally incident on 0.1 μm SiO_2.
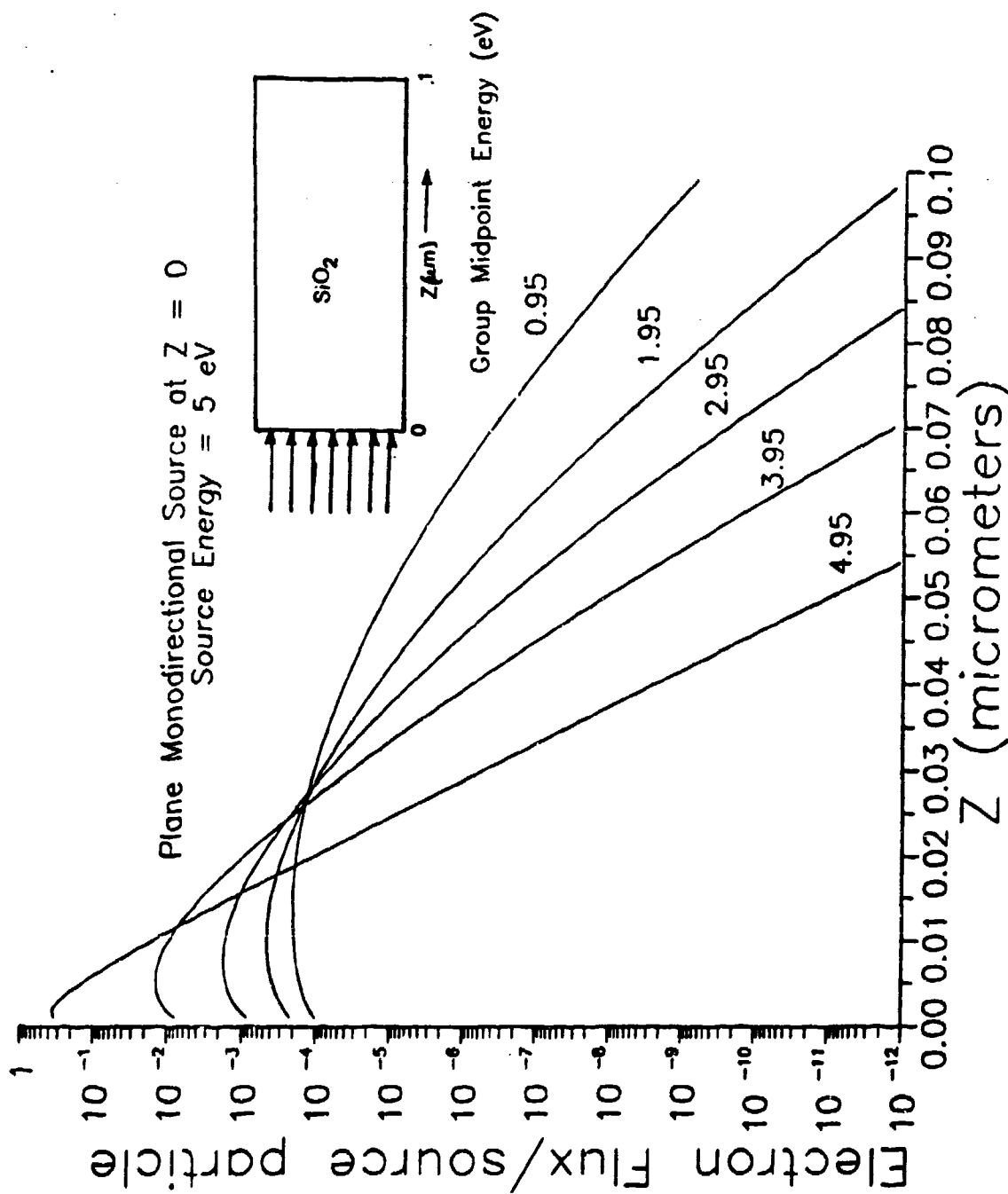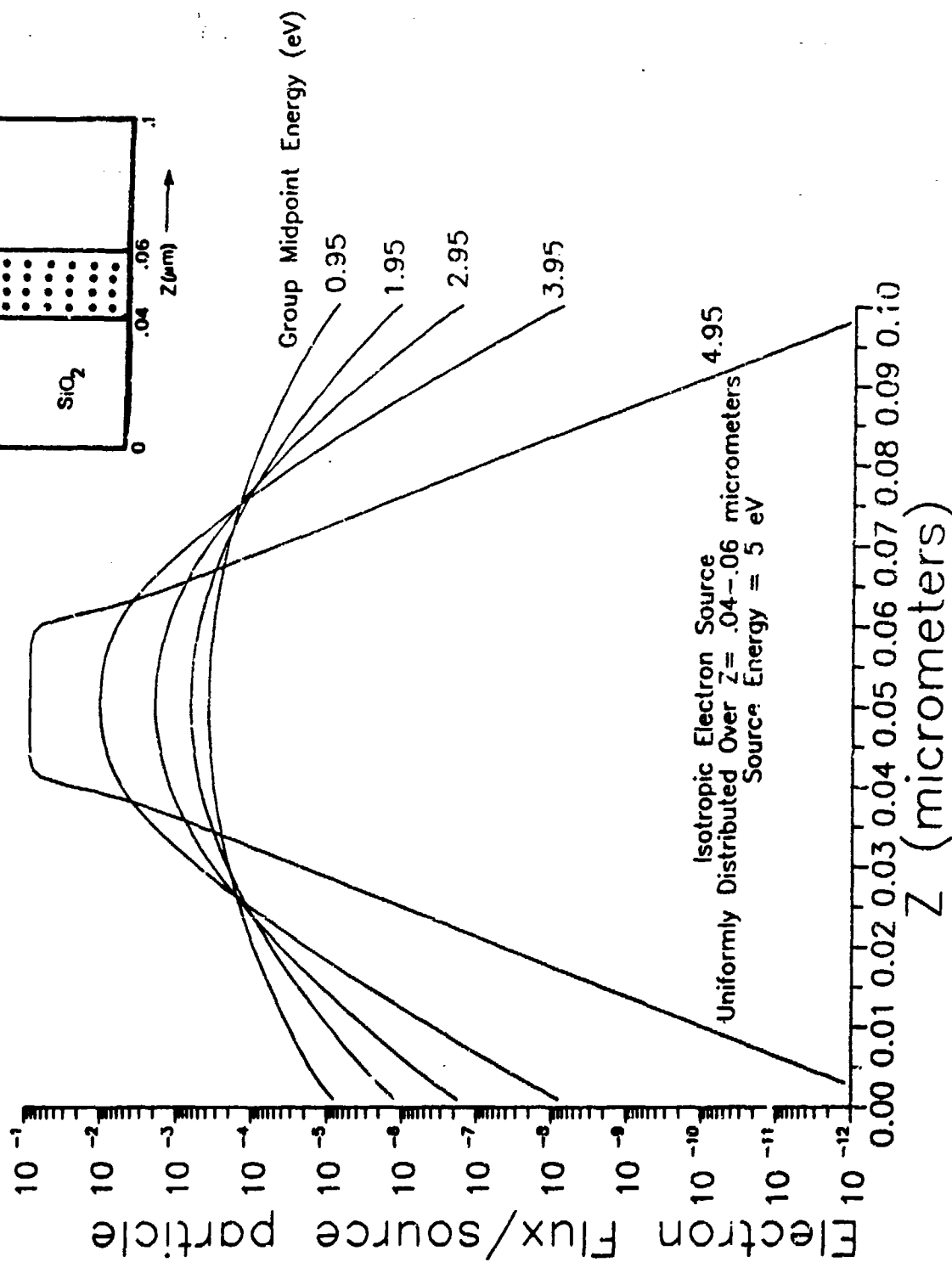
63

Figure 37. Electron flux vs. depth profiles, as calculated with ONETRAN[1] for electron-phonon scattering, for 5 electron energies, due to the presence of a 5 eV isotropic electron source uniformly distributed over the center region (0.04μm - 0.06 μm) in SiO₂ slab of thickness 0.1 μm.

4.4 S_n Treatment of Electron Transport in the Presence of an External Electric Field

Calculations of electron transport in the presence of an applied external electric field have been done by Wienke[29] using the method of discrete ordinates. We began the process of modifying our ONETRAN calculations to include an electric field term. We used as a theoretical basis the method outlined in Ref. 29.

The Lorentz force term, $\frac{e}{m_0 v}(\vec{E} + \vec{v} \times \vec{B}) \cdot \vec{\nabla}_v \phi$, is incorporated into the right-hand-side (source side) of the Boltzmann equation. The quantities e, m_0, v, $\vec{E}$ and $\vec{B}$ are, respectively, the electron charge, mass velocity, electric and magnetic fields. ϕ is the electron flux. For our purposes, the magnetic field portion was omitted. In this formulation, electric fields are treated as effective sources. The electric fields are regarded as having the effect of up- and down-scattering electrons in energy and also redistributing their directions. Slowing down and speeding up of electrons due to electric fields are treated in the continuous approximation(CSDA), i.e., only energy transfers between adjacent groups are allowed. Assuming slab geometry, Wienke's treatment of the Lorentz force source term (electric field portion only) proceeded as follows:

defining the direction cosine μ in one-dimensional plane geometry,

$$\vec{v} \cdot \vec{x} = vx\mu, \tag{57}$$

the gradient operator (velocity space) is given as

$$\vec{\nabla}_v = \frac{\vec{v}}{v} \frac{\partial}{\partial v} + (\frac{\vec{x}}{vx} + \frac{\mu \vec{v}}{v^2})\frac{\partial}{\partial \mu}, \tag{58}$$

one obtains

$$(\frac{e}{m_0 v})\vec{E} \cdot \vec{\nabla}_v \phi = (\frac{e}{m_0 v})[\mu E \frac{\partial \phi}{\partial v} + \frac{E}{v}(1 - \mu^2)\frac{\partial \phi}{\partial \mu}] . \tag{59}$$

The first term in [ ] above is the energy upscatter or downscatter term, depending on the direction of $\vec{E}$, while the second term in [ ] is the angular redistribution term. The first term can be expressed in finite difference form as

$$(\frac{e}{m_0 v}\mu E)\frac{\partial \phi_{gm}}{\partial v} = \epsilon(\frac{\mu}{\Delta v_g})(\phi_{g+1,m} - \phi_{gm}) , \qquad \text{for } \mu > 0 \tag{60}$$

and

65

$$\left(\frac{e}{m_o v}\mu E\right)\frac{\partial \phi_{gm}}{\partial v} = -\epsilon\left(\frac{\mu}{\Delta v_j}\right)(\phi_{g-1,m} - \phi_{gm}), \qquad \text{for } \mu < 0 , \qquad (61)$$

where, as in Fig. 34, $E_j > E_{g+1}$ and $\epsilon = \left(\frac{e}{m_o v}E\right)$.

The subscript m denotes the direction of the m-th discrete ordinate, μ_m. Both cases above contribute a positive downscattered or upscattered source to group g in the direction m. The upscatter terms necessitate outer (energy) iterations in the S_n calculation.

The angular redistribution term, $\frac{\partial \phi}{\partial \mu}$, was treated as a within-group collision (self-scatter) term. Since in S_n calculations, the angular dependence of the flux is expressed in terms of a Legendre series expansion of order M-1 in μ, it is advantageous to make use of the fact that

$$(1-\mu^2)\frac{\partial P_l}{\partial \mu} = \frac{l(l+1)}{(2l+1)}(P_{l-1} - P_{l+1}) \qquad (62)$$

in the flux expansion, so that

$$\left(\frac{eE}{m_o v^2}\right)(1-\mu^2)\frac{\partial \phi_{gm}}{\partial \mu} = \sum_{l=0}^{M-1}(2l+1/4\pi)\epsilon_g^l \phi_g^l P_l(\mu_m) - \epsilon_g^0 \phi_{gm} , \qquad (63)$$

with $\qquad \epsilon_g^0 = \frac{\epsilon}{v_j}\left[\frac{(2M^2 - 2M - 1)}{(2M+1)(2M-3)}\right]$ and $\epsilon_g^l = \epsilon_g^0 - \frac{\epsilon}{v_j}\left[\frac{(2l^2 - 2l - 1)}{(2l-1)(2l+3)}\right] .$ $\qquad (64)$

The extended transport correction of order M-1 was used in the electric field expansion.

When the above expressions were incorporated into the discrete ordinates form of the transport equation, all of the terms containing ϕ_{gm} are then transposed to the left-hand side (removal terms)of the transport equation and grouped into the total loss term , $\sigma_g \phi_{gm}$, with the appropriate modification of the total cross section (σ_g). The remaining source terms involving group-to-group transfer and angular redistribution will be grouped on the right-hand side (gain terms)of the transport equation with the in-group source, the fixed source, secondary electron source and inelastic downscatter source.

Since Wienke states in Ref. 29 that the analysis described above can be used to modify existing S_n codes, we began the process of incorporation of the electric field terms into our S_n calculations. This work is presently in progress. We believe that the use of another S_n code,

rather than ONETRAN, may be preferable. We have a code which, unlike ONETRAN, directly calculates electron fluxes (rather than flux Legendre moments), and makes direct use of the source terms (rather than their Legendre representation). Such a code may prove more suitable for the incorporation of electric field terms than ONETRAN.

V. References

1. T.R. Hill, "ONETRAN: A Discrete Ordinates Finite Element Code for the Solution of the One-Dimensional Multigroup Transport Equation", LA-5990-MS, Los Alamos National Laboratory (1975).

2. J.A. Halbleib, T.A. Mehlhorn and R.P. Kensek, "ITS 2.1 : Integrated TIGER Series of Coupled Electron/Photon Monte Carlo Code System", ORNL RSIC Computer Code Collection Package No. CCC-467, March 1988.

3. G.J. Lockwood, L.A. Ruggles, G.H. Miller, J.A. Halbleib, "Calorimetric Measurement of Electron Energy Deposition in Extended Media--Theory vs. Experiment", Sandia National Laboratories Report No. SAND79-0414, January, 1980.

4. A. R. Frederickson and S. Woolf, "Electron Beam Current Penetration in Semi-Infinite Slabs", *IEEE Trans. Nuc. Sci.* NS-28, No. 6., 4186, (1981).

5. J.C. Garth and S. Woolf, "Comparison of ONETRAN Calculations of Electron Beam Dose Profiles with Monte Carlo and Experiment", *IEEE Trans. Nuc. Sci.*, NS-34, No.6., 1551, 1987.

6. J. J. Duderstadt and W. R. Martin, Transport Theory, Pp. 479 ff., Wiley, New York (1979).

7. D.W.O. Rogers and A.F. Bielajew, "Differences in Electron Depth-Dose Curves Calculated with EGS and ETRAN and Improved Energy-Range Relationships", Med. Phys. 13, 687 (1986).

8. L. J. Lorence, Jr., W.E. Nelson and J.E. Morel, "Coupled Electron-Photon Transport Calculations Using the Method of Discrete Ordinates", *IEEE Trans. Nuc. Sci.* NS-32, No. 6., 4416, (1985).

9 . R.D. Evans, *The Atomic Nucleus*, McGraw-Hill, New York, 1955, Chap. 20.

10. H. W. Koch and J. W. Motz, *Rev. Mod. Phys.*, 31, No. 4, 920 (1959).

11. D. H. Rester, "An Experimental Study of Electron Transmission and Bremsstrahlung Production", National Aeronautics and Space Administration Report No. NASA CR-1383 (August 1969).

12. R. H. Pratt, *Phys. Rev.*, A19, 1525 (1979).

13. L. Kissel, C. MacCallum and R. H. Pratt, "Bremsstrahlung Energy Spectra from Electrons of Kinetic Energy 1 keV $\leq T \leq$ 2000 keV Incident on Neutral Atoms $1 \leq Z \leq 92$", Sandia National Laboratories Report No. SAND81-1337 (August 1981).

14. J. H. Renken and K. G. Adams, "An Improved Capability for Solution of Photon Transport Problems by the Method of Discrete Ordinates", Sandia Laboratories Report No. SC-RR-65-739 (December 1969).

15. F. Biggs and R. Lighthill,
    a) "Analytical Approximations for X-Ray Cross Sections", Sandia Laboratories Report No. SC-RR-68-619 (1968).
    b) "Analytical Approximations for Total Pair-Production Cross Sections", Sandia Laboratories Report No. SC-RR-68-619 (1968).
    c) "Analytical Approximations for X-Ray Cross Sections II", Sandia National Laboratories Report No. SC-RR-71-0507 (1971).

16. M. J. Berger and S.M. Seltzer, "Stopping Powers and Ranges of Electrons and Positrons", U.S. Dept. of Commerce, National Bureau of Standards Rept. No. NSBIR 82-2550, 1982.

17. M. J. Berger, Methods in Computational Physics, Vol.1, Academic Press, (1963).

18. H. A. Bethe, Handbuch der Physik, Vol. 24/1, Springer (1933).

19. W. L. Filippone, M. S. Smith, S. Woolf and J.C. Garth, Nucl. Sci. Eng. 95, 22 (1987).

20. W.L. Filippone, Nucl. Sci. Eng., 99, 232 (1988).

21. a) W.L. Filippone and S. Woolf, "Smart Scattering Matrices for Single Collision Electron Monte Carlo Calculations", Proc. Int'l. Top'l. Mtg. on Advances in Reactor Physics, Mathematics and Computation, 1, 389 (April 1987).
    b) W.L. Filippone and S. Woolf, Nucl. Sci. Eng., 100, 201 (1988).

22. W.L. Filippone, S. Woolf and J.C. Garth, "Two-Dimensional Transport Equation Calculations of Dose Profiles Due to Electron Beam Irradiation", IEEE Trans. Nuc. Sci. NS-34, No. 6., 1564, (1987).

23. W.L. Filippone, S. Woolf and J.C. Garth, "Smart First Collision Sources for Electron Transport Calculations", Trans. Am. Nuc. Soc.,55, 356 (1987).

24. W.L. Filippone, S.P. Monahan, S. Woolf and J.C. Garth, "Three-Dimensional Multiregion S_n Solutions of the Spencer-Lewis Electron Transport Equation", Proc. Top'l. Mtg. on Nuclear Engineering Computation and Radiation Shielding,2, 47, (April 1989).

25. S. Verghese, J. J. Wortman and S. E. Kerns, IEEE Trans. Nucl. Sci., NS-34, 1641(1987).

26. W. T. Anderson et al., IEEE Trans. Nucl. Sci., NS-34, 1326 (1987).

27. J. C. Ashley, Oak Ridge National Laboratory Health and Safety Research Division, Private Communication, (November, 1986).
    These results follow from the works of:
    a) M. Sparks et al., Phys. Rev. B, 3519 (1981);
    b) M. Fischetti, Phys. Rev. Lett., 1755 (1984);
    c) M. Fischetti et al., Phys. Rev. B, 8124 (1985);
    d) D. DiMaria et al., Phys. Rev. Lett., 1284 (1986);
    e) Physics Today, 54, Review Article (October 1986);
    f) Physics Today, S-55, Review Article (January 1987).

28. S. Woolf and J. N. Bradford, "Monte Carlo Simulation and Analysis of Elastic and Inelastic Scattering of Electrons in Insulators", *IEEE Trans. Nucl. Sci.*, NS-34, No. 6, 1392 (December 1987).

29. B. R. Wienke, "ESN: One Dimensional Transport Module for Electrons", *J. Quant. Spect. Rad. Trans.*, 28, 311(1982).